Jagiellonian University

Faculty of Physics, Astronomy and Applied Computer Science

Department of Medical Physics

Characterization of melanoma cell spheroids by means of imaging techniques and positron annihilation lifetime spectroscopy

---

Doctoral dissertation

Hanieh Karimi

Supervisors:

Prof. dr hab. Pawel Moskal
Prof. dr hab. Ewa Stepien

Krakow, 2021

Wydział Fizyki, Astronomii i Informatyki Stosowanej
Uniwersytet Jagielloński

Oświadczenie

Ja, niżej podpisana, Hanieh Karimi (nr indeksu: 1159849), doktorantka Wydziału Fizyki, Astronomii i Informatyki Stosowanej Uniwersytetu Jagiellońskiego, oświadczam, że przedłożona przeze mnie rozprawa doktorska pt. „Characterization of melanoma cell spheroids by means of imaging techniques and positron annihilation lifetime spectroscopy" jest oryginalna i przedstawia wyniki badań wykonanych przeze mnie osobiście, pod kierunkiem Prof. dr hab. Pawel Moskal and Prof. dr hab. Ewa Stępień. Pracę napisałem samodzielnie.

Oświadczam, że moja rozprawa doktorska została opracowana zgodnie z Ustawą o prawie autorskim i prawach pokrewnych z dnia 4 lutego 1994 r. (Dziennik Ustaw 1994 nr 24 poz. 83 wraz z późniejszymi zmianami).
Jestem świadom, że niezgodność niniejszego oświadczenia z prawdą ujawniona w dowolnym czasie, niezależnie od skutków prawnych wynikających z ww. ustawy, może spowodować unieważnienie stopnia nabytego na podstawie tej rozprawy.

Krakow, dnia .....

podpis doktoranta .....

No matter how educated, talented, rich and cool you are, how you treat people ultimately tells all.

To my mom and dad for their endless kindness

Mommy, I learned patience and kindness from you , and Daddy you taught me how to be strong in every situation ,and happy even in difficulties. You are the best!

Acknowledgements

This project would not have been possible without the support of many people. I would like to express my deepest gratitude to my supervisors, Prof. Pawel Moskal and Prof. Ewa Stepien for their constant support, guidance, encouragement and assistance during my Ph.D studies which I will never forget. Their unassuming approach to research and science is a source of inspiration. I learned to be thoughtful, creative and independent, which are something I hope to carry forward throughout my career.

I am fortunate to have been a part of the J-PET group. I would like to thank whole the J-PET team and my colleagues in medical physics department and my lab mates for their support and kindness.

I also express my warm and heartfelt gratitude to my family for their constant love and support keep me motivated and confident. My accomplishments and success are because they believed in me. Without that hope, this thesis would not have been possible. Thank you all for the strength you gave me.

This work was supported by the Foundation for Polish Science through grant TEAM POIR.04.04.00-00-4204/17 program to Prof. Pawel Moskal, Polish Ministry of Science and Higher Education grant No. N18/DBS/000007 to Prof. Małgorzata Przybyło and DSC grants No. N17/MNS/000023/2019, N17/MNS/000023/2020 ,and SciMat No. U1U/P05/NO/03.28 to Hanieh Karimi.

Achievements

List of author's full-papers

1. Dulski K, ..., **Karimi H**, et al. The J-PET detector—a tool for precision studies of ortho-positronium decays. Nuclear Instruments and Methods in Physics Research Section A: Accelerators, Spectrometers, Detectors and Associated Equipment. 2021. IF=1.46(2020). MNISW: 70 points.

2. Moskal P, ..., **Karimi H**, et al. Testing CPT symmetry in ortho-positronium decays with positronium annihilation tomography. Nature communications. 2021. IF=14.92(2020). MNISW: 200 points.

3. Moskal P, ..., **Karimi H**, et al. Positronium imaging with the novel multi-photon PET scanner. Science advances. 2021. IF=14.14(2020). MNISW: 200 points.

4. **Karimi H**,..., et al. X-ray microtomography as a new approach for imaging and analysis of tumor spheroids. Micron. 2020. IF=2.25(2020). MNISW: 100 points.

5. Stępień E, **Karimi H**, et al. Melanoma spheroids as a model for cancer imaging study. Acta Physica Polonica. B. 2020. IF=0.75(2020). MNISW: 40 points.

6. Sharma S, ..., **Karimi H**, et al. Estimating relationship between the time over threshold and energy loss by photons in plastic scintillators used in the J-PET scanner. EJNMMI physics. 2020. IF=3.31(2020). MNISW: 100 points.

7. Moskal P, ..., **Karimi H**, et al. Performance assessment of the 2 γ positronium imaging with the total-body PET scanners. EJNMMI Physics. 2020. IF=3.31(2020). MNISW: 100 points

8. Moskal P, ..., **Karimi H**, et al. Synchronization and Calibration of the 24-Modules J-PET Prototype With 300-mm Axial Field of View. IEEE Transactions on Instrumentation and Measurement. 2020. IF=5.08(2020). MNISW: 140 points.

Contents

Abstract **x**

List of abbreviations **xi**

1 Introduction **1**

I Theoretical background **4**

2 Tissue engineering **5**

2.1 Melanoma 5

2.2 3D cell culture 5

2.2.1 Difference between mono layer cell culture and 3D cell culture 7

3 Nutrient diffusion in a spheroid **10**

3.1 Glucose uptake 10

3.2 Hypoxia and malignancy 12

4 Imaging technique **14**

4.1 Micro-tomography 14

5 Positron annihilation lifetime spectroscopy **16**

5.1 Positron annihilation spectroscopy 16

5.2 Positron and Positronium 16

5.3 Annihilation phenomenon 18

5.4 Tao-Eldrup model 19

6 Thesis objectives **21**

II Materials and Methods **23**

7 Spheroid generation and characterization using bio luminescence and imaging techniques **24**
7.1 Cell culture 24
7.2 Hanging drop method 25
7.3 Biochemical staining techniques 25
7.4 Micro-CT imaging 26

8 Determination of nutrient diffusion in spheroids **28**
8.1 Glucose distribution 28
8.2 Hypoxia region in spheroids 30

9 PALS technique **32**
9.1 5D spherical plates 32
9.2 Viability test assay 33
9.3 Spectrometer 34
9.4 Radioactive source 36
9.5 Holder and chamber of spheroids 37
9.6 Positron annihilation lifetime spectroscopy in 3D spheroids . . . 39

10 Data analysis and Image processing **41**
10.1 Statistical analysis 41
10.2 Bruker software 41
10.3 Analysis of positron annihilation lifetime spectra 44
10.3.1 Charge and Amplitude computation 44
10.3.2 The time difference 46
10.3.3 Positron lifetime calculation 46
10.3.4 Gain callibration 48

III Results **51**

11 Determination of Spheroid characteristics using biochemical and imaging techniques **52**
11.1 The rate of growth and shape analysis 52
11.2 Viability 56
11.3 Microtomography imaging 59

12 Determination of nutrient diffusion in spheroids using bioluminescence techniques **60**
12.1 2-NBDG uptake monitoring in 3D melanoma spheroids using confocal microscopy 60
12.2 Determination of a hypoxic region 64

13 Determination of positronium lifetime in melanoma spheroids with different malignancy level **67**
13.1 Spheroid morphology and proliferation rate 67
13.2 Spheroids' cells characterisation 69
13.3 The lifetime of o-Ps 70

IV Discussion **73**

14 Discussion **74**
14.1 Spheroid characteristics 74
14.2 Positronium lifetime 77

15 Conclusion **80**

Bibliography **82**

Abstract

The presented thesis is devoted to evaluating the three-dimensional (3D) spheroid characteristics using imaging techniques and examining the positron annihilation lifetime spectroscopy (PALS) as a novel biomedical approach to identify the cancer malignancy level.
A 3D spheroid mimics important properties of a real tumor and may soon become a reasonable substitute for animal models and human tissue. In this thesis, the morphological analysis of spheroid cell cultures was conducted using micro-CT and compared to that of confocal microscopy. An approach is proposed that can potentially open new diagnostic opportunities to determine the characteristics of cancer cells cultured in 3D structures instead of using actual tumors. Micro-CT analysis of a spheroid showed that the spheroid size and shape differed depending on the cell line, initial cell number, and duration of culture. The micro-CT allows for high-resolution visualization of the spheroids' structure.
In this study, it was hypothesized whether the difference between the grade of malignancy of cancer cell lines can be probed by positronium biomarker. The hypothesis was tested on the 3D spheroid model. Positron annihilation lifetime spectroscopy is known as an appropriate technique to evaluate the properties of different organic and inorganic materials based on the determination of the void size within and between molecules.
To test the proposed hypothesis, the lifetime of ortho-Positronium (o-Ps) was evaluated in 3D melanoma spheroids from two melanoma cell lines differing in the stage of malignancy. Obtained results show that the o-Ps lifetime and intensity are different between 3D melanoma spheroids with different malignancy level. The presented method paves the way for the application of the 3D spheroids for the *in-vitro* tests of positronium biomarker. The result of the method applied to studies of positronium in melanoma cancer cells revealed that positronium is a promising biomarker that may be applied in PET diagnostics for the assessment of the degree of cancer malignancy.

List of abbreviations

DBS - Doppler broadening spectroscopy

EDTA - Ethylenedinitrilotetraacetic acid

FBS - Fetal bovine serum

FDA - Fluorescence diacetate

GLUT - Glucose transporters

HIF - hypoxia inducible factor

MCTS - Multicellular tumor spheroids

NBDG - N-(7-Nitrobenz-2-oxa-1, 3-diazol-4-yl) Amino)-2-Deoxyglucose

o-Ps - ortho-Positronium

OCT - optical coherence tomography

PALS - Positron annihilation lifetime spectroscopy

PBS - Phosphate-buffered saline

PET - Positron Emission Tomography

PI - Propidium iodide

PMT - photo-multiplier tube

p-Ps - para-Positronium

PTA - phosphotungstic acid

RPMI - Roswell Park Memorial Institute

SGLT - Sodium-glucose cotransporters

SPECT - Single Photon Emission Computed Tomography

Chapter 1

Introduction

Over the past few decades, three-dimensional (3D) cell cultures also called 3D spheroids have been widely used as *in vitro* models which can bridge the gap between *in vitro* and *in vivo* cell conditions. The comparison of the 3D cell culture to a cell monolayer revealed specific physiological and morphological characteristics such as cell-to-cell, and cell-matrix interactions, cell signaling, proliferation and necrosis [1, 2].

Unlike a monolayer cell culture, the 3D spheroid is an appropriate model to mimic the real tumor cell environment and the nutrient diffusion rate between cells. Indeed, there are different approaches for generating 3D cell culture and there is a need to select the appropriate method regarding a cell line, cell media and matrices. Spheroid generation can be applied using different methods such as scaffold free and scaffold based methods which having their own variety and modifications [3, 4]. Multicellular tumor spheroids (MCTS) allow researchers to understand the biochemical mechanism of cell growth, enzymatic reactions, and various treatment modalities [5, 6].

Melanoma is a prevalent type of skin cancer that has been categorized as one of the most lethal cancers [7]. The rate of metastasis in patients due to melanoma is high, 350,000 new cases per year, and the number of new cases is significantly increasing each year [8–10]. Different melanoma cell lines, WM266-4 and WM115, can form scaffold-free spheroids using methods such as a hanging drop method, while melanocytes, normal skin cells, generate spheroids using scaffold-based methods which need bio materials such as chitosan, agarose, collagen, etc., helping cells gather and form the 3D cell culture [6, 11].

X-ray microtomography (micro-CT) is a non-destructive and well-suited method for the visualization of internal structures and the analysis of small

samples that provides spatial resolution at the micron level. Over the last decade, micro-CT has become a gold standard in pre-clinical imaging and has been particularly useful in the pre-clinical investigation of calcified tissues and organs such as bones and teeth [12, 13].

Calcified tissues contain elements with high atomic number (Z). X-rays are absorbed by these tissues very well, thereby producing a good image contrast. Conversely, differences in X-ray attenuation between soft tissues are minimal and the overall attenuation effect is similar to that observed for water, creating a very weak contrast of soft tissue images. However, the image quality can be significantly improved using several staining methods.

The idea of staining originated from histological studies, but micro-CT requires more of the contrasting solution because of high sample volumes. The success of micro-CT visualization depends on molecular diffusion of contrast agent into the tissue. The staining time is longer and might even take up to weeks for large samples. The most common staining protocols use Lugol solution (I_2 , KI), osmium tetroxide (OsO_4) or phosphotungstic acid (PTA) [14–16].

Recently the studies dedicated to various aspects of positronium in cancer diagnostics have been discussed. Positronium is a bound state of an electron and positron and shows a high potential in providing information about material structure in a nano and sub-nanoscale [17, 18]. Positron is a physical particle similar to an electron but with a positive charge. During interaction with an electron, positron can annihilate into two gamma quanta with 511 keV energy or create positronium. Positronium can exist in 2 states, p-Ps and o-Ps which decay with the mean lifetime of 0.125 ns, and 142 ns respectively [18,19].

Lifetime and intensity of o-Ps vary in different environments and free volumes. Therefore, o-Ps can be used in medical diagnostics to find out beneficial information about the sub-micro environment properties [17, 18]. Regarding positronium function in defects and free spaces, the positronium annihilation lifetime can provide information about the geometric changes at the molecular level [20].

In this thesis, in the first step the 3D melanoma cell culture characteristics has been evaluated using bio luminescence techniques and micro-CT imaging to visualize the internal and external structure of spheroids. In next step, the lifetime of o-Ps has been studied in two different melanoma spheroids with different malignancy rate, WM266-4 as a malignant melanoma cell line, and WM115 as a primary melanoma cell line. These studies were conducted to test whether cancer cells in different stages have different molecular properties

which can be determined by the measurement of the lifetime of o-Ps.

The uptake rate of essential nutrients such as glucose and oxygen in cancer cells is different than in normal cells and in cancer cells it depends on the malignancy rate [21]. Therefore in this thesis, the rate of glucose and oxygen uptake has been also investigated to show the dependency of o-Ps lifetime on milieu characteristics.

This thesis is divided into four parts, in theoretical background the 3D spheroid's characteristics, imaging techniques and the Positron Annihilation Lifetime Spectroscopy(PALS) are described. Materials and methods applied for 3D spheroid generation, microscopic and micro-CT imaging, as well as PALS measurement and data analysis are presented in Part 2. Part 3 is devoted to the results of the experiments in which spheroid's properties were determined using biochemical approaches and imaging, bioluminescence techniques and PALS. In part 4, discussion and conclusion are included.

Part I

Theoretical background

Chapter 2

Tissue engineering

2.1 Melanoma

Melanoma is the most dangerous type of skin cancer and remains the main cause of skin cancer-related deaths. The incidence of melanoma is rapidly increasing with approximately 350,000 new cases reported worldwide each year [8]. Globally, the prevalence of melanoma skin cancer is predicted to show an increase of 18% with 340,271 cases and the rate of death will rise to 72,886 cases in 2025 an increase of 20% [22, 23].

Melanoma is a multi-factorial disease in which both genetic susceptibility and environmental exposure, predominantly to ultraviolet light, play important roles [24]. The appointed environmental risk factors for melanoma cancer are exposure to solar ultraviolet radiation(UVB) and sunburns(UVA). UVB persuades direct DNA damage in which leads to DNA strand breaks. UVB also promotes melanoma cell survival, angiogenesis, and invasion due to increases in the penetration of macrophages and neutrophils into skin cells. UVA causes DNA damage through the production of free radicals which induce oxidative stress in melanocytes. The risk for melanoma can also be associated with inherited mutations and somatic mutations, but the genetic tendency is responsible for only a small number of cases. As the effectiveness of melanoma treatment at advanced stages is low, there is a constant need for the development of new targeted therapies, immunotherapy, and combined therapies [7].

2.2 3D cell culture

For decades, animal models and 2D *in vitro* cultures were the standard approaches for determining biological effect that molecules and therapeutic drugs

in different types of diseases, including cancer. Over the past two decades, however, several new methods such as nanobiosensors, multicellular 3D spheroids and radioactive carries have been developed to evaluate biological activity in cancer [1].

One of the most promising preclinical *in vitro* methods introduced in recent years, are 3D spheroids as they can mimic the structure of tumors under physiological conditions. Tumor 3D spheroids hold certain benefits over standard research approaches, together with high reproducibility, time-saving, low cost of use, and reduce the necessity for laboratory animal models [4, 25].

The distinctive properties of 3D tumor spheroids create them priceless for biological experiments and drug tests during a type of experimental studies centered on therapy and radiation therapy [3]. A typical spheroid is a three-layered structure and each cell layer has a different proliferation rate. The proliferation rate of spheroids varies at different developmental stages just as observed in solid tumors. Several methodlogies are often accustomed turn out 3D spheroids such as liquid overlay, hanging drop, rotary vessel bioreactors, and spinner flask methods [26, 27]. Compared to alternative strategies, the hanging drop cell culture is the commonest because it doesn't need any special instrumentality, and is straightforward to perform [28].

The size of the spheroids in each experiment depends on the initial cell-seeding density. In general, lower cell seeding densities, 10cells/drop, form small spheroids ranging from 37-40 μm^2 and a bigger number of initial cells, 100 cells/drop generate 281-300 μm^2 spheroids over the time. The spheroids can grow to the diameter of 500 μm or more using more initial cell density [6, 26]. The deepest layer of a spheroid forms a necrotic core; the middle layer contains a quiescent layer, and the external layer is called the proliferating rim. The specificity of layers is explained by the level of the oxygen and access to nutrients as well as the removal of metabolic waste because of completely different diffusion rates at intervals specific layers [4, 29]. Figure 2.1 represents a schematic view of a 3D spheroid with multi-layer structure.

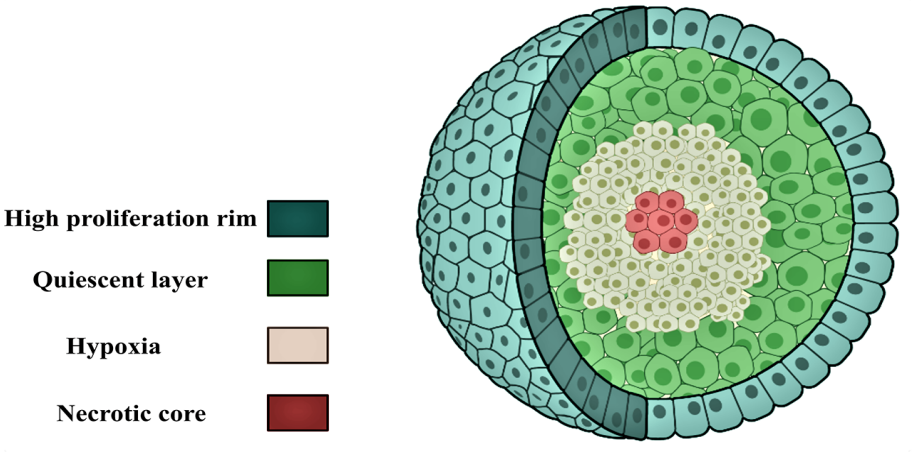

Figure 2.1: Schematic view of a multi-layer 3D spheroid. Figure is created using Biorender.com [30].

2.2.1 Difference between mono layer cell culture and 3D cell culture

The first cell culture was introduced in 1907 by Harrison researched on nerve cells and the neural 3D cell cultures were introduced by Stepien in 1997 [31–33]. 2D cell culture has been the most common *in vitro* approach to study cell biology, tissue function, drug responses and tissue engineering development. This cell culture model is easily available, fast reproducible and low cost. Although 2D cell cultures have some advantages, they do not imitate the tumor characteristics or tissue natural structure. Therefore, 3D cell cultures were made for the first time in 1970 by Hamburg and Salmon to compensate the 2D cell culture limitations [34, 35].

2D cell culture has a monolayer structure where cells grow in a culture dish on a flat surface with a contact with surface of culturing plate and medium, and limited interaction with neighbor cells, Fig. 2.2. They attache to the surface of the plate and divide at a special doubling time. Due to unlimited access to essential nutrients and oxygen, cells in 2D cell culture are in the same condition for proliferation and growth [34]. They have limited cell-cell and cell-matrix interactions and these differences turn back to different gene expression and protein metabolism.

In contrast to monolayer cell culture, cells in 3D cell culture system grow on the top of each other and form the spherical and multilayer structure similar to *in vivo* tumor, Fig 2.1, Fig 2.2. The morphology of cells in 3D spheroids is alike real tumor cells. The proliferation rate in different layers of 3D cell

Figure 2.2: 2D and 3D cell cultures. Figure is created using Biorender.com [30].

culture is different due to different accessibility to nutrients and oxygen. Cells which are located in outer layer of spheroid have suffiecient access to nutrients while in the inner part of the spheroid, the accessibility to oxygen and vital substances is decreasing gradually [5].

In 3D spheroids, unlike 2D cell cultures, cells have suitable cell-cell and cell-matrix interaction allowing cells to imitate the tumor structure. Some genes such as collagen 1 and fibrinogen have higher expression in the 3D cell culture matrix. The localization of specific proteins such as integrin $\beta 1$ can affect the cell polarity and increase the tumor metastasis potential [2, 36, 37]. 3D spheroids have similar gene expression, metabolism and cell signaling as real tumor cells [38]. Table 2.1 shows 2D and 3D cell culture characteristics in a comparison model.

Characteristics and differences of 2D and 3D cell culture models		
	2D	3D
Structure	mono layer, homogeneous, flat	multi layer, heterogeneous, solid
Cell characteristics	no *in vivo*-like morphology, cells grow on a flat surface, have a flat shape and single layer, loss of divers division time and polairty	*in vivo*-like morphology, multi layer and 3D structure, divers doubling time and polarity in different layers
nutrient accessibility	unlimited access to nutrient and oxygen	various accessibility to essential nutrients depends on the distance from the surface.
cell-cell interactions	limited cell-cell and cell-matrix interactions	appropriate cell-cell and cell-matrix interactions
Molecular mechanism	diverse gene expression, topology and biochemical metabolism	similar gene expression, topology and biochemical metabolism to *in vivo*
in vivo emulation	no imitation of natural tissue structure	similar structure as *in vivo*
culture properties	simple, long-term culturing, fast reproducibility, cheap, easy interpretation, available	more complicated, slow reproducibility, more expensive, difficult to interpret, short-term culturing

Table 2.1: Comparison of 2D and 3D cell culture characteristics

Chapter 3

Nutrient diffusion in a spheroid

As a spheroid grows in diameter, the cell number is increasing; therefore the spheroid requirements for essential nutrients such as glucose and oxygen are increasing due to an increase in the number of cells over the time and competition between cells for receiving sufficient nutrients for cell growth. A 3D spheroid exhibits a heterogeneous structure due to its multilayered composition. This heterogeneity occurs not only on a cellular level but also as a metabolic aspect [39]. Owing to this heterogeneity, cells in different layers of a 3D spheroid have different sizes, DNA content, proliferation ability, and metastasis possibility [40, 41]. Their cell cycle is also differentially regulated. Most of these alterations occur due to nutrient deprivation [42]. Accessibility to nutrients is changing significantly within the cell distance from the surface of a spheroid. By moving towards the center of a spheroid, the rate of glucose, ATP, and oxygen will decrease while the amount of lactate, CO_2 and waste will increase. The concentration of different nutrients in a spheroid depends on the cell type, cell characteristics, and size of the spheroid [41]. In this part of the thesis, the relation between the structure of cancer spheroids and the distribution of metabolic substrates such as glucose and oxygen has been studied.

3.1 Glucose uptake

Glucose is a monosaccharide molecule utilized as one of a main energy source for a different types of cells. Glucose exists in two forms: D or L [43, 44]. Most cells, except for some gram-negative bacteria, catabolize only D-glucose which due to its molecular structure can easily enter the cells. The hexokinase is an enzyme which can fold to the three-dimensional structure of D-glucose.

The active site of hexokinase is completely fit with D-glucose structure, while L-glucose can not be matched with this enzyme. D-glucose is metabolised in human body *via* glycolysis and the pentose phosphate pathway. As a result of glycolyse, pyruvic acid, NADH, ATP molecules and water are formed. Owing to L-glucose inability to enter into the cells, L-glucose can be used as a marker for extracellular space and an indicator of cellular integrity in both *in vitro* and *in vivo* studies [45, 46]. The uptake of D-glucose is performed either passively *via* some transporters located on the cell surface called the GLUT family or actively through Na/glucose linked transporters (SGLT), Fig. 3.1.

The rate of glucose uptake is different between normal and cancer cells. Normal cells obtain glucose and metabolize it in mitochondria *via* an oxidative phosphorylation process called respiration, while in cancer cells most of energy from glucose is provided *via* glycolysis which occurs in cytoplasm. Thus, cancer cells utilize a faster process for metabolizing glucose than normal cells. Therefore, measurement of the rate of glucose uptake provides information about its metabolism in cells, particularly in cancer cells [43, 45].

The rate of glucose uptake depends on over-expression of GLUTs genes and their presence on the surface of cells [47]. Monitoring glucose transport inhibitors [48] and identifying the GLUTs translocation modifications can be possible by determining the rate of glucose uptake [49]. Variety of factors influence the glucose uptake such as high number of GLUTs transporters, insulin, and the existence of hypoxia region in tumor [47, 49, 50]. Among them, the high concentration of GLUTs transporters increases the rate of glucose uptake by enabling to enter the glucose molecules into the cells *via* facilitated diffusion [51]. Insulin stimulates energy storage and utilization by increasing the regulated glucose transportation into the cells. Insulin increases glucose uptake by enriching the concentration of GLUTs transporters on the cell membrane [52]. The expression of GAPDH and ENO1 enzymes is significantly increased under hypoxia conditions, which led to the glycolysis. HIF-1α is a protein that is produced during hypoxia condition and significantly attenuate glycolytic enzyme expression [50]. The decreases in insulin release in response to hyperglycemia, which is maintained with glucose infusions, is associated with the decline in potassium level. On the other hand, K^+ decreases glucose uptake. There is an inverse relationship between potassium level and the rate of glucose uptake [53, 54].

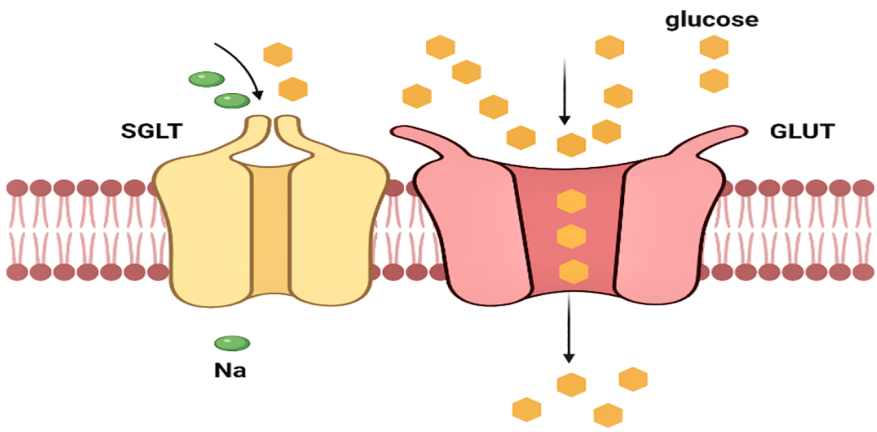

Figure 3.1: Schematic view of how glucose molecules enter a cell. GLUT (glucose transporter) is a membrane protein which is responsible for transporting the glucose molecules into the cells *via* simple fusion. SGLT(Na^+/glucose linked transporter) is a membrane transporter which mediate the simultaneous transportation of glucose and Na^+ into the cells *via* active transportation. Figure is created using Biorender.com [30].

3.2 Hypoxia and malignancy

Hypoxia is one of the most important features of cancerous tumors. Hypoxia is defined as imbalance between oxygen demand and oxygen supply. In clinical situation, hypoxia has important implications as increase of tumor progression, metastasis, development of drug resistance and resistance to radiation therapy [55]. Due to lack of nutrients and oxygen, a necrotic core is formed in deeper layer of tumors(150-200μm).

In the hypoxic region the growth factor secretion is induced which let to angiogenesis [56]. Hypoxia-inducible factor (HIF) promotes the invasion, metastasis [55] and treatment failure [57,58]. Another consequence of hypoxia is pH lowering in the extracellular environment that is caused by producing lactic acid that can promote metastasis [59,60]. During HIF activation, the rate of E-cadherin declines and the invasion probability is increased because E-cadherin limits tumor migration and metastasis [61]. In contrary, by reduction of hypoxia and lack of HIF, the glycolytic and acidosis processes are suppressed; therefore the cell death will be boosted by therapeutic techniques. HIF protein does not exist in normal conditions due to the presence of a proteasome system that degrades the HIF proteins. Under hypoxic conditions, some specific proteasome inhibitors such as Lactacystin and MG-132 are expressed which

protect the HIF complex in cells from degradation [62]. Figure 3.2 illustrates the schematic view of how hypoxia can influence cancer cells.

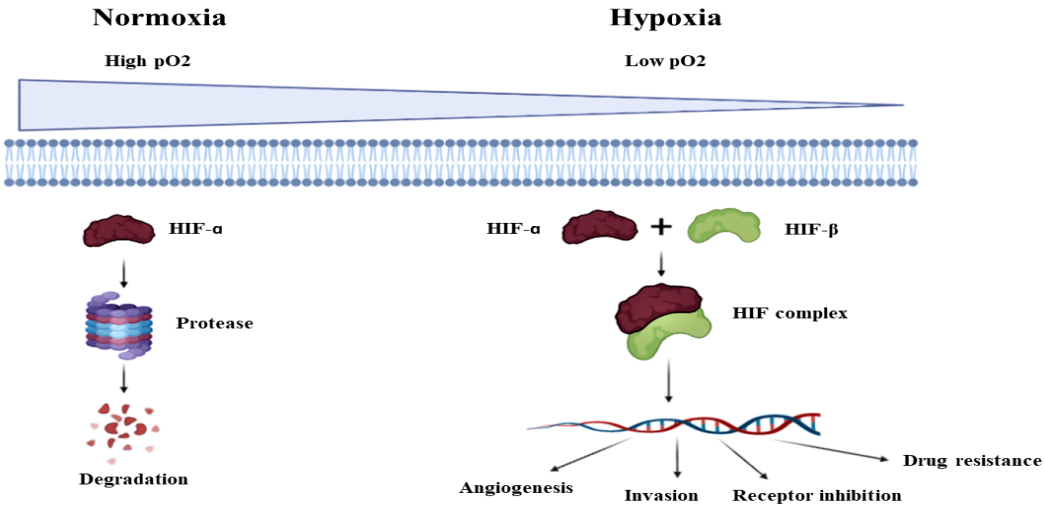

Figure 3.2: Schematic view of HIF effects on cancer cells. HIF (hypoxia-inducible factor) is a transcription factor that normally exists in cell cytosol. In normoxia condition, HIF is degraded by Proteosome passway, which is an enzymatic process while under hypoxia condition, HIF subunites, $HIF-\alpha$ and $HIF-\beta$, make a complex and enter the nucleus. HIF complex can target the special parts of the human genome and induces or suppresses the genes and causes some events such as angiogenesis, invasion, metastasis, receptor inhibition, and cell death. Figure is created using Biorender.com [30].

Chapter 4

Imaging technique

4.1 Micro-tomography

Micro computed tomography (Micro-CT) is an X-ray imaging technique which allows getting information about the inner structure of the specimen on a micro scale. Micro-CT is a rapid technique that gives results within minutes up to several hours. It has high sensitivity to bone and calcified tissues and can provide high resolution images. The reconstruction, analysis, and interpretation of results in 2D and 3D formats is simple. The specimen is rotated 180 or 360 degree producing a series of 2D images with spacial resolution of 1-2 μm per pixel. These 2D projection images are then reconstructed using a computer software to produce three-dimensional images. These series of images are typically called the reconstructed images or cross sections [16, 63].

Although micro-CT scanning has the same principle as medical Computed Tomography(CT) imaging system, it differs in some properties and design. In micro-CT, sample is rotating and X-ray source is fixed while in medical CT, the patient lies on a bed and X-ray tube rotates around the patient, Fig 4.1. Medical CT imaging is not appropriate for very dense specimen due to lower power(10 W) while micro CT is able to provide high qualified images from dense samples owing to more power(up to few kW) [64]. Figure 4.1 illustrates the schematic view of medical CT and micro-CT differences.

A typical medical CT scanner performs a scan within a few seconds while a micro-CT scan can be completed in 80 seconds for low-density samples, and up to 14 hours for high-density specimens. Medical CT scanner provides medical information about the inner parts of the human body for clinical use while micro-CT which works at micron level is used for materials science, and small animal imaging [65]. Figure 4.1 shows the process of imaging by means

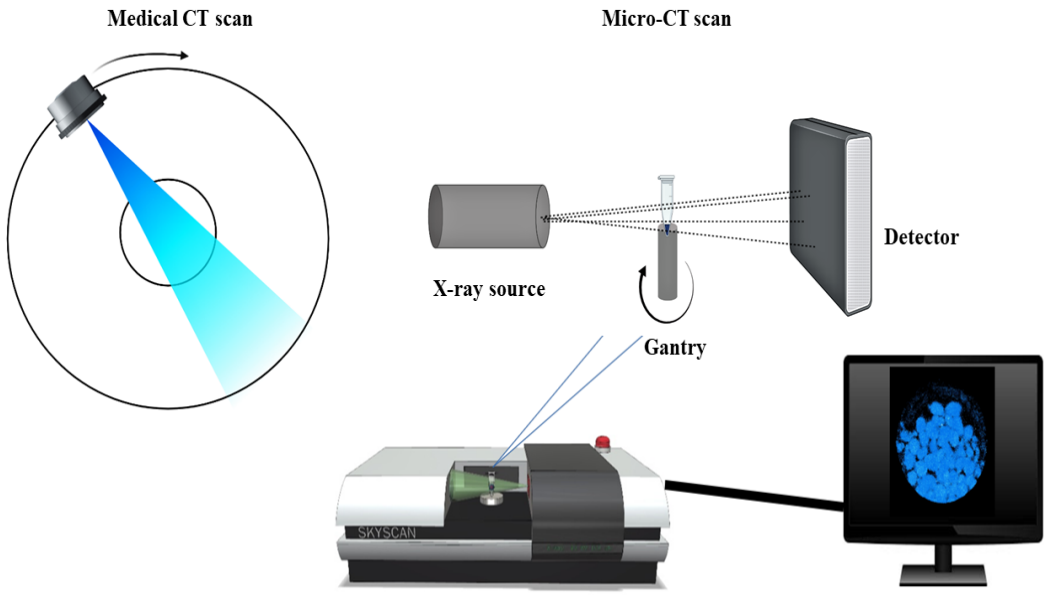

Figure 4.1: Schematic view of medical CT scan and micro-CT scan comparison. Figure is created using Biorender.com [30].

of micro-CT imaging system. The Visualization of micro-CT and CT scan images can be improved using special materials called contrast agent such as Iodine. Contrast agent can make better differentiation between organs and soft tissue. These materials can increase the attenuation difference between a target and surrounding [66].

Iodine is a micro-CT contrast agent with a brown color liquid which can be prepared as a solution. As follows, 10 parts of potassium iodide, then 5 parts of iodine are diluted in 85 parts of water (I_2 , KI). In solution, iodine (I_2) and potassium iodide (KI) form iodine trimers (I_3) and potassium ions (K^+). Although the staining principles remain poorly understood, it is clear that the iodine trimers bind to carbohydrates such as glycogen and glyco-lipids, which are naturally present in soft tissues. Through experimental evaluation of different type of contrast agents for use in micro-CT studies, it was demonstrated that Lugol's iodine (I_2 KI) solution can be considered as the best one in these imaging system. This is due to its high atomic weight which compensate the lack of inherent contrast for soft tissue imaging, and due to effective differentiating between target and surrounding and easy bounding with molecules in cells [67].

Chapter 5

Positron annihilation lifetime spectroscopy

5.1 Positron annihilation spectroscopy

Positron Emission Tomography (PET) is an advanced medical imaging technique for diagnosing different types of diseases such as cancer. It works by detecting back-to-back gamma photons emitted *via* electron–positron annihilation inside the body after administration of radiopharmaceuticals. Positron annihilation lifetime spectroscopy(PALS) is a technique used to study voids and defects in materials. Combination of simultaneous PET and PALS referred to as Positronium Imaging [68] is a novel approach in cancer diagnosis which shows high potential in providing information about nano- molecular structure and concentration of the bioactive molecules *in vivo* [18, 68].

In this thesis, positron annihilation lifetime spectroscopy (PALS) is used as it is the most prevalent positron spectroscopy allowing to determine the molecular characteristics of different substances. A positron is a physical particle similar to an electron but with a positive charge. During interaction with an electron, positron can annihilate into two gamma quanta with the energy of 511 keV or create positronium. Positronium can exist in 2 states, para-Positronium (p-Ps) and ortho-Positronium (o-Ps) which decay with the mean lifetime of 0.125 ns, and 142 ns respectively [69, 70].

5.2 Positron and Positronium

Positron is an anti-electron particle and it possesses the same characteristic as electron except for charge while positronium is a metastable bound state

	mass	spin
positron	510.998 keV	1/2
positronium	1.022 MeV	0 (p-Ps), 1(o-Ps)

Table 5.1: Positron and Positronium properties

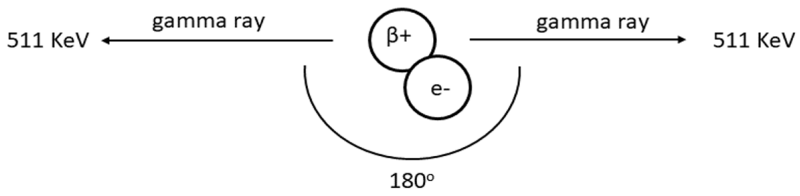

Figure 5.1: positron-electron interaction

of electron and positron, Table 5.1. Positron can be produced by β^+ emitting radioisotopes during their decay or pair-production of high-energy gamma rays. There are different radioactive sources emitting positrons such as ^{64}Cu and ^{58}Co but in PALS, the most commonly applied source is ^{22}Na with a half-life of 2.6 years, decaying into ^{22}Ne. ^{22}Na decays *via* the following process:

$$^{22}Na \rightarrow ^{22}Ne^* + \nu + e^+ \rightarrow ^{22}Ne + \gamma + \nu + e^+$$

Where excited $^{22}Ne^*$ nucleus de-excites *via* emission of γ with the energy of 1274 keV with the mean lifetime of about 3ps [71]. The measurement of the emission time of the γ gives the information about the time of emission of a positron, hence the formation of positronium, while the time of the decay of positronium is determined by the measurement of 511 keV photons originating from the positronium annihilation.

Positronium exists in two states depending on the spin S, p-Ps(singlet state, S=0) or o-Ps(triplet state, S=1), Table 5.1. Figure 5.1 shows the interaction of one positron and electron following the production of two gamma quanta with an energy of 511 keV. Owing to a conservation laws, p-Ps emits 2 γ quanta while o-Ps emits 3 γ quanta during their annihilation [72], Table 5.2.

Conservation law for positron annihilation	
Charge conversation	$e^+ + e^- = 0$
Energy conservation	$oPs : E^+ + E^- = E_{\gamma_1} + E_{\gamma_2} + E_{\gamma_3}$ $pPs : E^+ + E^- = E_{\gamma_1} + E_{\gamma_2}$
Momentum conservation	$oPs : p^+ + p^- = p_{\gamma_1} + p_{\gamma_2} + p_{\gamma_3}$ $pPs : p^+ + p^- = p_{\gamma_1} + p_{\gamma_2}$
Charge conjugation	$oPs : -1 = -1_{\gamma_1} \cdot -1_{\gamma_2} \cdot -1_{\gamma_3}$ $pPs : +1 = -1_{\gamma_1} \cdot -1_{\gamma_2}$

Table 5.2: Conservation law in positron annihilation phenomenon

5.3 Annihilation phenomenon

During positron passage through the material, positron thermalizes by losing its kinetic energy through ionization and excitation of material molecules. After thermalization, positron may annihilate directly with an electron or it may create positronium. Positron annihilation can occur *via* different processes such as:

- Intrinsic decay of positronium:
  Intrinsic decay shows the positronium annihilation in a vacuum when one positron and electron collides with each other.
- Ortho - para conversion:
  This process demonstrates the interaction of positronium with paramagnetic molecules(M) in the material (*via* process: $oPs + M \rightarrow pPs + M$) which decreases the mean lifetime of o-Ps.
- Pick-off process:
  Pick-off process describes the shortening of o-Ps lifetime due to the annihilation of positron from positronium with a surrounding electron in a matter.
- Direct annihilation of positron:
  This phenomenon occurs when a thermalized positron does not bound to an electron. Therefore positron directly annihilate with a surrounding electron into two γ quanta with energy of 511 keV.

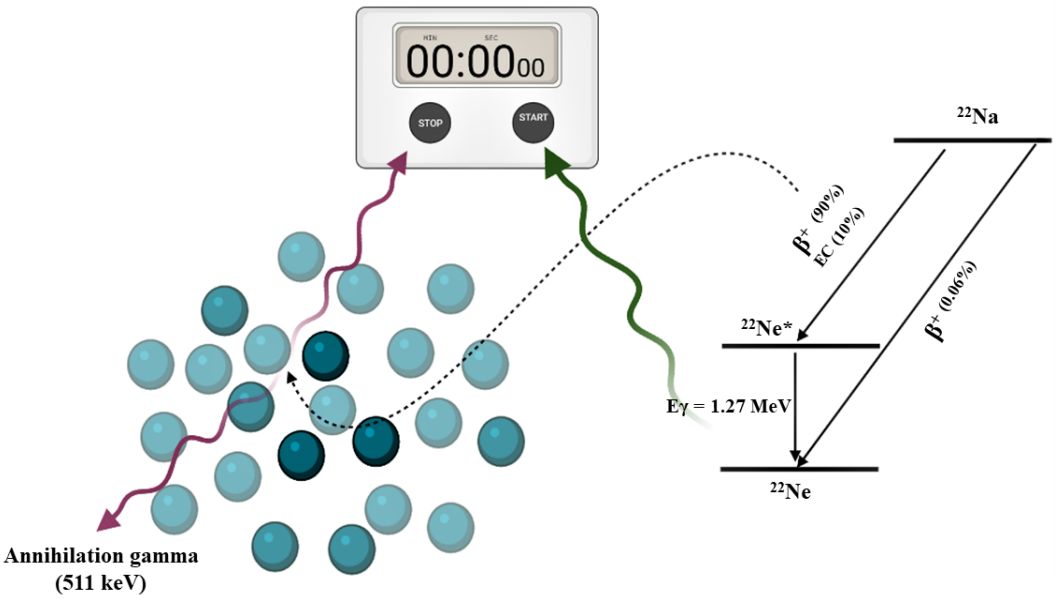

Figure 5.2: Schematic view of positron annihilation phenomenon. Figure is created using Biorender.com [30]

As mentioned before, positronium exists in 2 states: p-Ps and o-Ps with the creation rate of 1 to 3, respectively. Both positroniums are unstable and annihilate into photons. In vacuum: p-Ps with 0.125 ns and o-Ps with 142 ns mean lifetime. The o-Ps atom produces 3 γ quanta in vacuum while it may also decay into 2 γ quanta in a dense environment, owing to pick-off and conversion processes [17].

Regarding the lifetime of positronium, the size of the free spaces and voids can be calculated according to the Tao-Eldrup model. The bigger the void is, the longer the o-Ps lifetime is [73–75].

5.4 Tao-Eldrup model

The relationship between the mean lifetime of o -Ps and intra-molecular free volumes have been described by the Tao-Eldrup model. In this model, free voids between the molecules have been considered as the low electron density regions in which positronium can be trapped and decay [76]. It is frequently assumed that the voids have the spherical geometry, therefore the probability of finding the positronium in the voids can be estimated *via* (Eq. 5.1):

$$P = 4\pi \int_R^\infty |\psi(r)^2| r^2 dr \tag{5.1}$$

The dependency of mean positronium lifetime value and void radius has been formulated in (Eq. 5.2) [77]:

$$\tau_{ps} = \frac{1}{2}(1 - \frac{R}{R + \triangle R} + 2\pi sin(\frac{2\pi R}{R + \triangle R}))^{-1} \tag{5.2}$$

where R is the void radius, τ_{ps} is the mean lifetime of positronium and $\triangle R$ is a parameter equal to 0.166 nm. Tao-Eldrup model is valid for spherical voids and is used for voids with radius up to 2 nm. The lifetime of positronium from 1.8 ns to 6.2 ns has correlation to the voids with the radius between 0.2 nm and 2 nm [75].

Chapter 6

Thesis objectives

The main goals of this Ph.D thesis are as follows:

1. The application of microtomography for imaging of small tumor-like structure composed from malignant and non-malignant melanoma cancer cells-spheroids

2. Evaluation of the glucose and oxygen uptake rate distribution in melanoma spheroids with different degree of malignancy.

3. Determination of positronium properties in experimental melanoma models (spheroids) for testing properties of cancer

To reach these goals, several new methods and protocols have been developed and evaluated:

1. Spheroid formation from two melanoma cell lines, WM115(primary) and WM266-4(metastatic)

2. Confocal and optical microscopes have been utilized to evaluate the spheroid proliferation, structure and morphology

3. Microtomography has been applied to characterize the physical properties of spheroids

4. Positron Annihilation Lifetime Spectroscopy (PALS) has been conducted to determine the mean lifetime of positronium in melanoma spheroids with

different malignancy level

The research hypothesis tested in this thesis state that the difference at the level of physiology between the melanoma cells with different grade of malignancy are reflected at the molecular level that can be probed by positronium.

Part II

Materials and Methods

Chapter 7

Spheroid generation and characterization using bio luminescence and imaging techniques

7.1 Cell culture

Two cutaneous melanoma cell lines obtained from the ESTDAB Melanoma Cell Bank (Tübingen, Germany) was used. These cell lines, WM115(primary) and WM266-4(metastatic) were derived from the same individual [78]. Cells were cultured in T75 cell culture flasks (GenoPlast. Biochemicals, cat. no 708011, Rokocin, Poland) with complete culture media, which consisted of Gibco Roswell Park Memorial Institute (RPMI) 1640 (Gibco, cat. no 21875091, Waltham, MA USA) supplemented with 10% fetal bovine serum (FBS) (Gibco, cat. no 10500064, Waltham, MA USA) and 1% penicillin streptomycin (Gibco, cat. no 15140122, Waltham, MA USA) and maintained in an incubator at 37 °C and 5% CO_2 with 95% humidity. Cells from passage 19–23 with the number of living cells higher than 90% in total cells were used to generate spheroids. A trypan blue assay with a Luna-II TM automated cell counter was used to perform cell counts and a viability tests prior to seeding cells.

7.2 Hanging drop method

In this study, the hanging drop method as a scaffold-free model was selected to determine the spheroid's characteristics [3, 4]. Drops were formed on the lids of 90 mm Petri dishes and the culture medium of each drop was changed every 48 h. Each cell line was seeded at a different cell density (500, 1000, and 1500 cells) in drops of 15 μl of RPMI medium. The bottom of each Petri dish was filled with 5 mL of PBS (Gibco, cat. no 10010056, Waltham, MA USA) to prevent drops from drying out and to provide humidity, Fig 7.1.

Spheroids were maintained under standard cell condition. Spheroids were formed after 24–48 h of incubation depending on the cell line. The morphology and growth of spheroids were assessed after 2, 5, and 7 days of spheroid growth. Spheroid morphology was determined by optical microscopy (Olympus, IX-LWPO, T2, Japan).

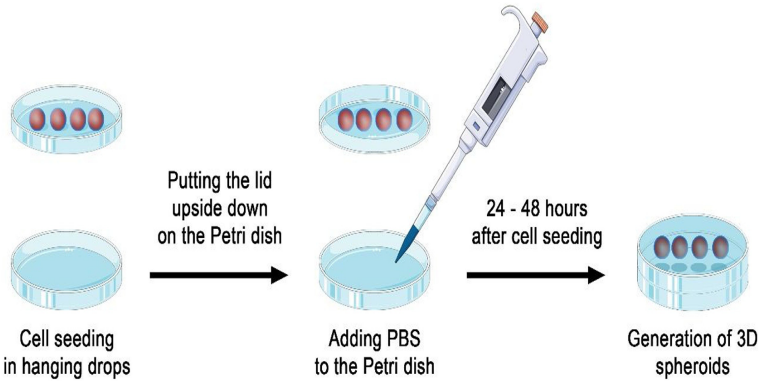

Figure 7.1: A graphical illustration of the formation of three-dimensional (3D) spheroids in Petri dishes using a hanging drop method [79].

7.3 Biochemical staining techniques

Cell viability was determined during spheroid formation by using three standard fluorescence dyes: red-fluorescent propidium iodide (PI) (SIGMA, cat. no P- 4170), green fluorescent fluorescein diacetate (FDA) (SIGMA, cat. no F-7378), and calcein (Thermo Fisher Scientific, cat. no C1430) in concentration: FDA (5 mg/mL) and calcein (1 mg/mL) for living and PI (0.4 mg/mL) for dead cells (chapter 11.2) .

To stain spheroids, a single spheroid was transferred from the petri dish to a glass-bottom dish and 100 μl of staining solution was added. The stained

spheroid was incubated at 37 °C for 10 minutes and then washed gently twice with PBS, Fig. 7.2. Thereafter, 100 μl of complete culture media was added to the spheroid before observation under an epifluorescence microscope. FDA and calcein can cross the membrane of living cells, while PI can only enter dead cells. The percentage of death cells has been calculated as a percentage of red fluorescence area. This method allows to evaluate the localization of dead and living cells within a spheroid.

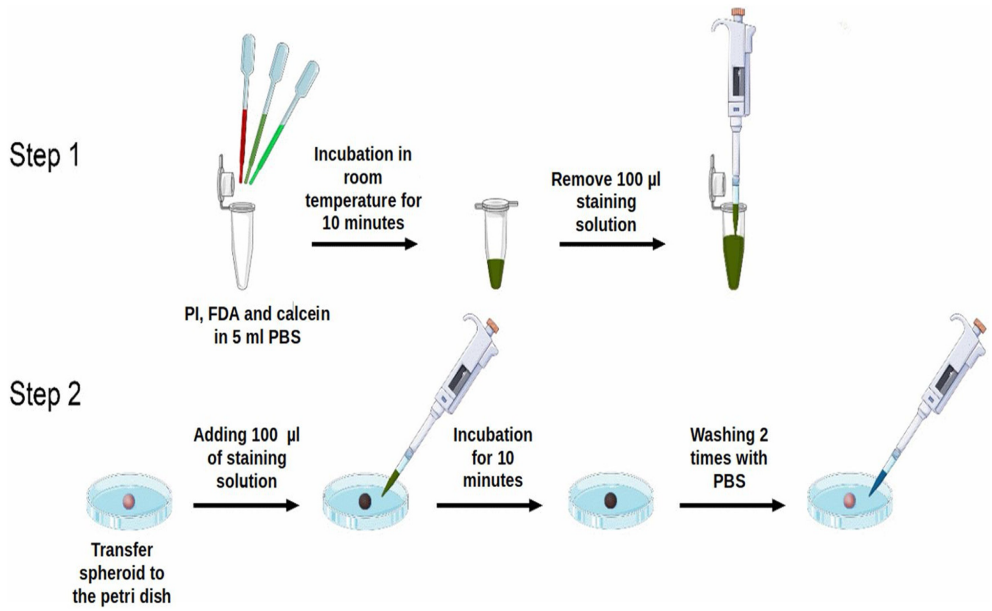

Figure 7.2: A schematic representation of the fluorescence microscopy triple staining protocol. Step 1: Preparation of the fluorescence staining solution. Step 2: Staining of a single spheroid [79].

7.4 Micro-CT imaging

Micro-CT analysis was carried out with a Bruker SkyScan 1172 scanner (Bruker microCT, Kontich, Belgium) and scanning parameters were set to 40 keV without physical filtration. Images were captured with a spatial resolution of 1-2 μm per pixel. To enhance the signal to noise ratio, each projection image was taken as the average of 10 frames.

Optimization of micro-CT staining included samples that were not fixed and samples that were fixed with 4% formaldehyde for 15 minutes. Standard micro-CT staining solutions, Lugol solution (SIGMA, cat. no 62,650) and 10% PTA (SIGMA, cat. no P4006), were used and the incubation period for

staining was experimentally optimized for between 30 minutes and 24 h. After staining, samples were washed with PBS and scanned. Figure 7.3 shows the schematic view of sample prepration for Micro-CT imaging.

Captured data was reconstructed and processed with Bruker software (Bruker microCT, Kontich, Belgium) Nrecon (v. 1.7.3.1) and CTanalyzer (v. 1.18.8.0+), respectively. An anisotropic diffusion filter was applied to reduce image noise and images were binarized by histogram-based global thresholding. Afterwards, the 3D watershed separation algorithm was used to separate individual clusters of the spheroid.

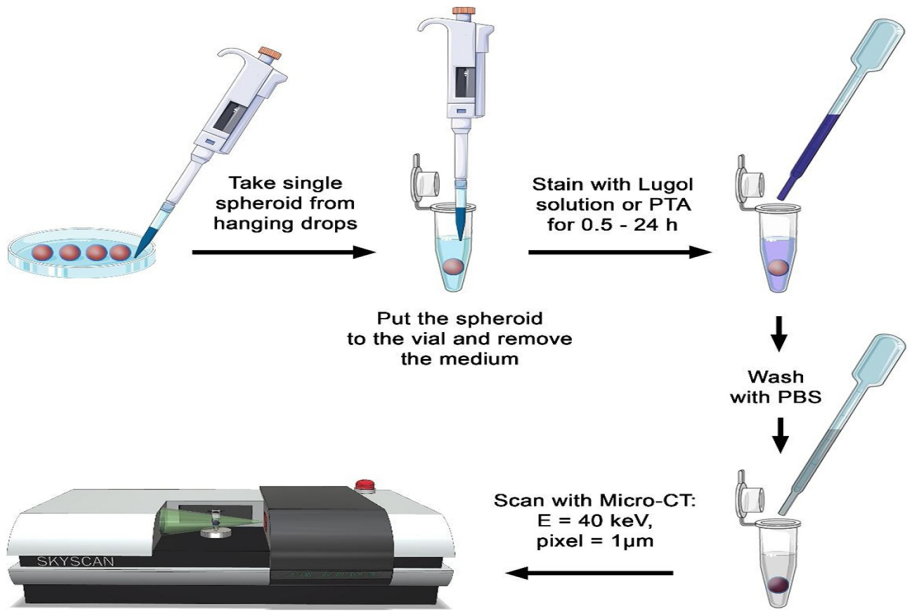

Figure 7.3: A schematic representation of the micro-CT protocol [79].

Chapter 8

Determination of nutrient diffusion in spheroids

8.1 Glucose distribution

This part of the thesis was considered to follow up the rate of glucose and oxygen uptake in WM266-4 and WM115 melanoma spheroids. The main aim of this research was to evaluate the glucose and oxygen distribution in melanoma spheroids and its relation to the level of malignancy. In order to evaluate glucose uptake dependency on the level of malignancy in melanoma spheroids, a fluorescence-emitting D-glucose probe was bound to D-glucose that could penetrate the cells. In this study, 2-NBDG (2-(N-(7-Nitrobenz-2-oxa-1, 3-diazol-4-yl) Amino)-2-Deoxyglucose) (Thermo Fisher Scientific, cat. no N13195) which is an effective D-glucose tracer to investigate the rate of glucose uptake inside cells with molecular formula $C_{12}H_{14}N_4O_8$ was used as a fluorescent glucose analog to evaluate the glucose rate distribution in melanoma spheroids, Fig. 8.1.

3D spheroids were created from two melanoma cell lines, (WM266-4, and WM115), seeded at a different cell densities: 1000 and 2000 cells/drop. A single spheroid was transferred from the Petri dish to a glass-bottom dish at 4 and 8 days after culturing. In the next step, the medium was completely removed from the spheroids and 20 μl of 2-NBDG dye (200 μM) was added to each single spheroid. Afterward, the spheroids were incubated for 45 minutes at 37 °C. Finally spheroid were rinsed with PBS gently and imaged by an inverted Nikon Eclipse Ti-E microscope coupled with an A1 scanning confocal system (Nikon, Japan) at 494 nm/551 nm fluorescent wavelength, Fig. 8.2. In this experiment, spheroids should not have medium during staining because

the medium is composed of glucose and it can interfere with binding the 2-NBDG probe to glucose absorbed by the cells.

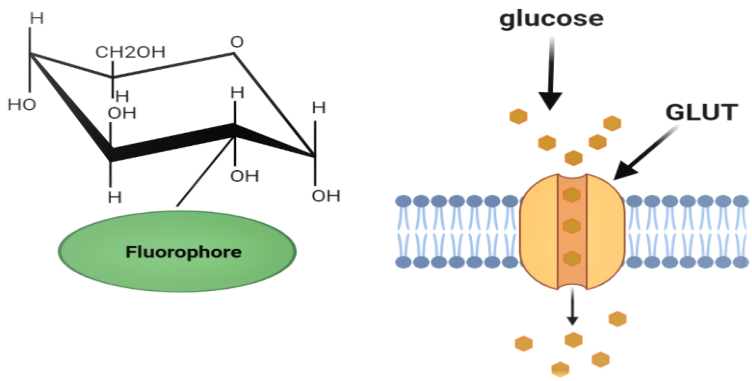

Figure 8.1: Schematic view of D-glucose labelling with a fluorophore molecule. The D-glucose structure is composed of 4 chiral carbon that carbon number 2 has one free space to link to other molecules such as fluorine atoms [80]. Figure is created using Biorender.com [30].

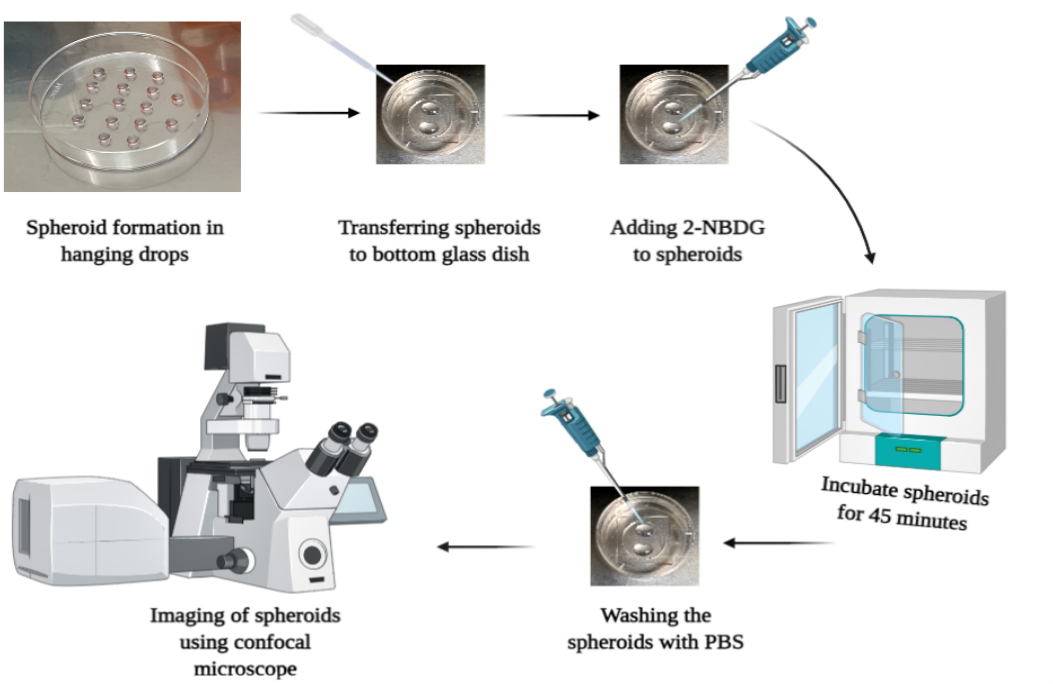

Figure 8.2: Staining protocol with 2-NBDG for glucose uptake evaluation. Figure is created using Biorender.com [30].

8.2 Hypoxia region in spheroids

In this thesis, the oxygen uptake rate distribution was determined using a hypoxia kit, Image-IT™ Green Hypoxia Reagent (Thermo Fisher Scientific, cat. no I14834). To evaluate the distribution of oxygen uptake rate in different melanoma spheroid layers, two different cell lines, (WM266-4 and WM115), were seeded at densities: 1000, and 2000 cells/drop. On days 4 and 8, the spheroids were transferred to glass-bottom dishes to investigate hypoxia in spheroids regarding the time of culturing and rate of malignancy.

In the next step, 20 μl of Image-IT™ Hypoxia Reagent (10 μM) was added to each spheroid. The spheroids were incubated at 37°C for 1 hour. Afterward, the hypoxia dye was exchanged with the fresh growth medium, and the spheroids were placed again in a cell culture incubator for next 4 hours. Spheroids images have been done by an inverted Nikon Eclipse Ti-E microscope coupled with an A1 scanning confocal system (Nikon, Japan) at 488 nm/520 nm fluorescent wavelength.

In this thesis, the hypoxia reagent with azo structure has been used to determine the hypoxic region in spheroids. An azo dye is a fluorescence molecule with the structure of an azo function group (R-N=N-R), where R is an aromatic ring compound bonded to a nitrogen [81], Fig. 8.3.

Figure 8.4 presents the schematic view of the staining process for hypoxia region detection.

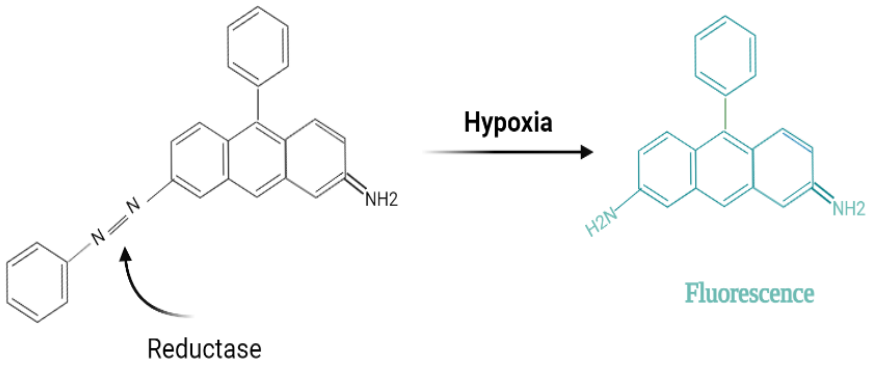

Figure 8.3: The process of reductive cleavage in azo dye. An azo dye can be fluorescent when reductive cleavage occurs. In the normoxic condition and sufficient supply of oxygen, the reduction of azo group is suppressed therefore azo dye is non fluorescent while under hypoxia and oxygen limitation, azo bound will be reduced and become fluorescent due to the increased amount of reductase [81, 82].

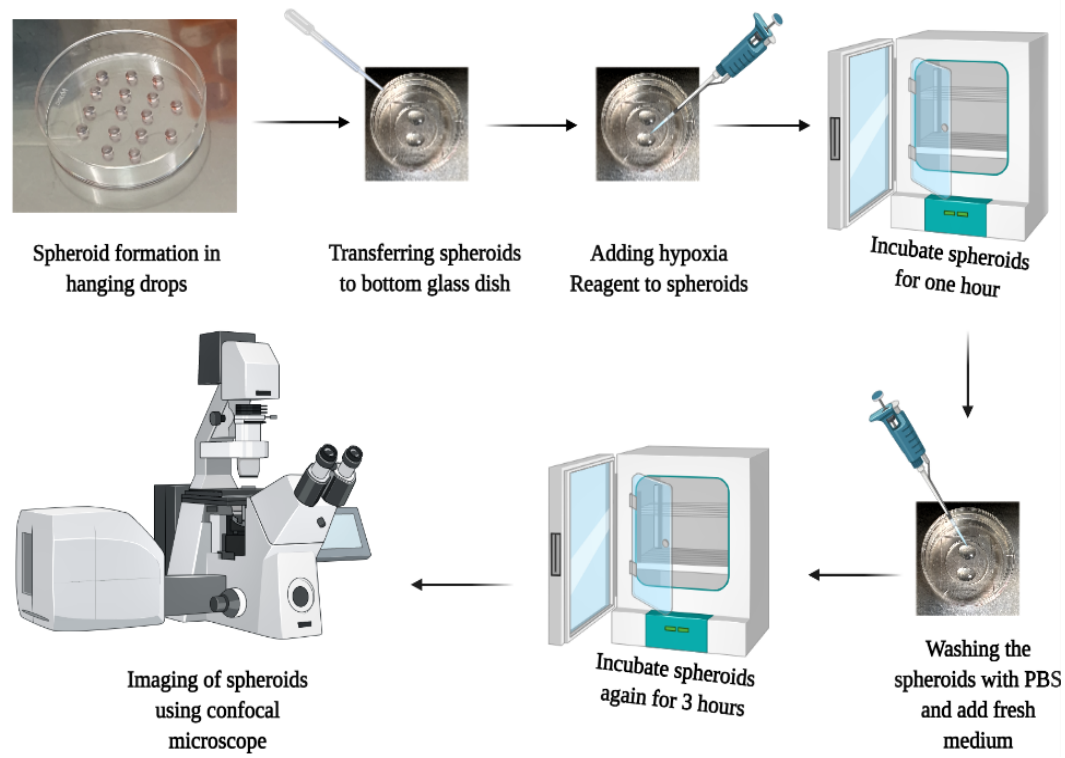

Figure 8.4: Schematic view of staining protocol with hypoxia reagent for investigation of hypoxic region in 3D spheroids. Figure is created using Biorender.com [30].

To determine the rate of glucose and oxygen uptake in a spheroid, images from a spheroid with a "Maximum Intensity" projection and the best focus have been saved in a TIFF format. Then, the bright field image of each spheroid has been evaluated to quantify the fluorescence distribution of glucose and oxygen probes in different layers of a spheroid. Thus, the center of a spheroid has been recognized and the distance from the center to the edge of a spheroid has been considered as the radius of a spheroid. Afterward, for each spheroid, 5 different regions at the same distances from the center of the spheroid were specified using the ImageJ software. The fluorescence intensity, as a function of distance from the spheroid surface, 50 μm by 50 μm, was calculated by averaging the intensities of the same distance regions in a spheroid. This method decreases the location-related variability in a spheroid [83, 84].

Chapter 9

PALS technique

9.1 5D spherical plates

In this part of the thesis, 5D sp5dplates, Kugelmeiers, Switzerland were used to form spheroids. The 5D microplate has 24 wells, 12 wells for the spheroid formation, and 12 wells as control. Each well contains 750 microcavities that are separated from each other by sharp borders and these borders prevent cell migration from one microcavity to another one, thus 9000 spheroids with uniform shape and diameter can be cultured in a single plate. Each microwell had the shape of reversed pyramid with the base of 509 μm and height of 320 μm .

For cell seeding, firstly 0.5 ml complete medium was added to each well. Then extra 0.5 ml medium including 1 125 000 cells/well (1500 cells/microwell) was added to each well of the plate. The cells in the falcon were resuspended to distribute them in the whole medium and then added to the wells. Due to the gravity, cells sediment on the nanocoated surface of each microwell. To avoid evaporation during incubation, 12 control microwells were filled with PBS to provide humidity for cells as it is presented pictorially in Fig 9.1.

After cell seeding, cell culture medium was renewed every day after the spheroids were formed. Two suitable time points of spheroid growth were chosen to measure the mean o-Ps lifetime. Spheroids morphology and proliferation rate were also determined under the optical microscope (Olympus, IX-LWPO, T2, Japan) at 4th and 8th days after cell seeding. Image analysis was conducted by ImageJ software.

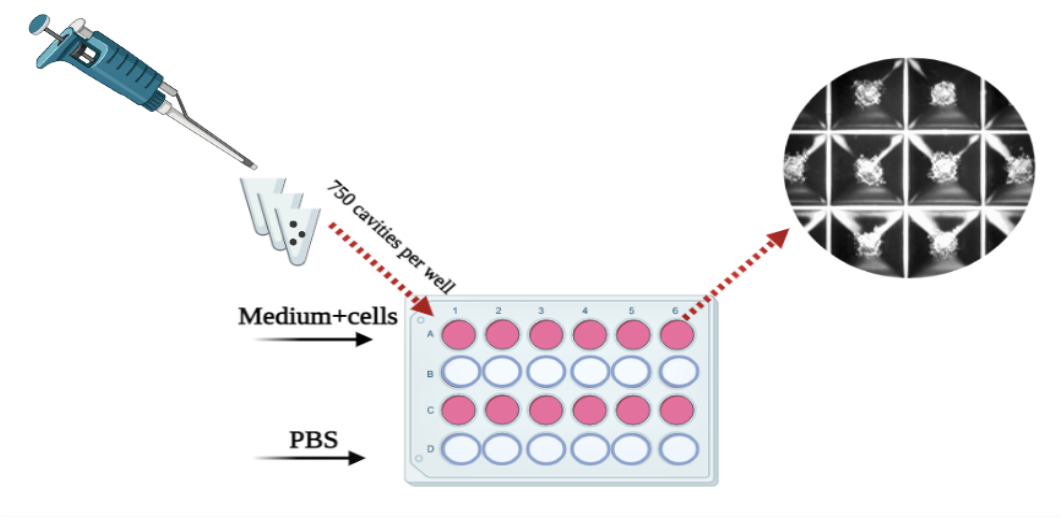

Figure 9.1: Spheroid formation using 5D microplate. Spheroids were formed 2 to 3 days after cell seeding depending on the cell line. The upper right picture shows spheroids inside part of microcavities (with 509 µm diameter and 320 µm depth. Figure is created using Biorender.com [30].)

9.2 Viability test assay

Firstly, spheroids were dissociated to single-cell suspension with trypsin/EDTA (cat. no. 25200072, Waltham, MA USA). 100µl of trypsin/EDTA Spheroids were incubated for 10-20 minutes at 37 °C and pippeted several times to separate cells. Then cells were centrifuged at 300 g for 3 min, the supernatant was removed, 100µl medium (Gibco, cat. no. 10010056, Waltham, MA, USA) was added to cells and pippeted several times to separate cells completely. In the final step, 10µl of cells were added to 10µl trypan blue and counted using Luna-II TM cell counter. The workflow is shown in Figure 9.2.
After 15 minutes in the incubator, the cells were checked to ensure there were no aggregates. After the viability test using the cell counter, the cell cluster map has been evaluated to see the percentage of clusters. In our experiments, cluster maps showed a high percentage of dissociation, above 90%.
Afterward, the size of cells for both cell lines in 3D shape has been checked by cell counter and microscopic investigations. For estimation of the cell size, Luna II TM cell counter has been used. Regarding the histogram of size distribution, the mean diameter of cells was estimated. For the comparison, the size of cells in 2D cultures was also determined. For this purpose, spheroids were removed from each well using a 3 ml pipette, with a large bore to not destroy

the spheroids' structure. Then spheroids were poured onto a 15ml Falcon (cat. no. 601052NEST/G66010522, GenoPlast, Biochemicals) and centrifuged in 500 g for 7 minutes. In the next step, the supernatant was removed, and 1ml fresh medium added to spheroids.

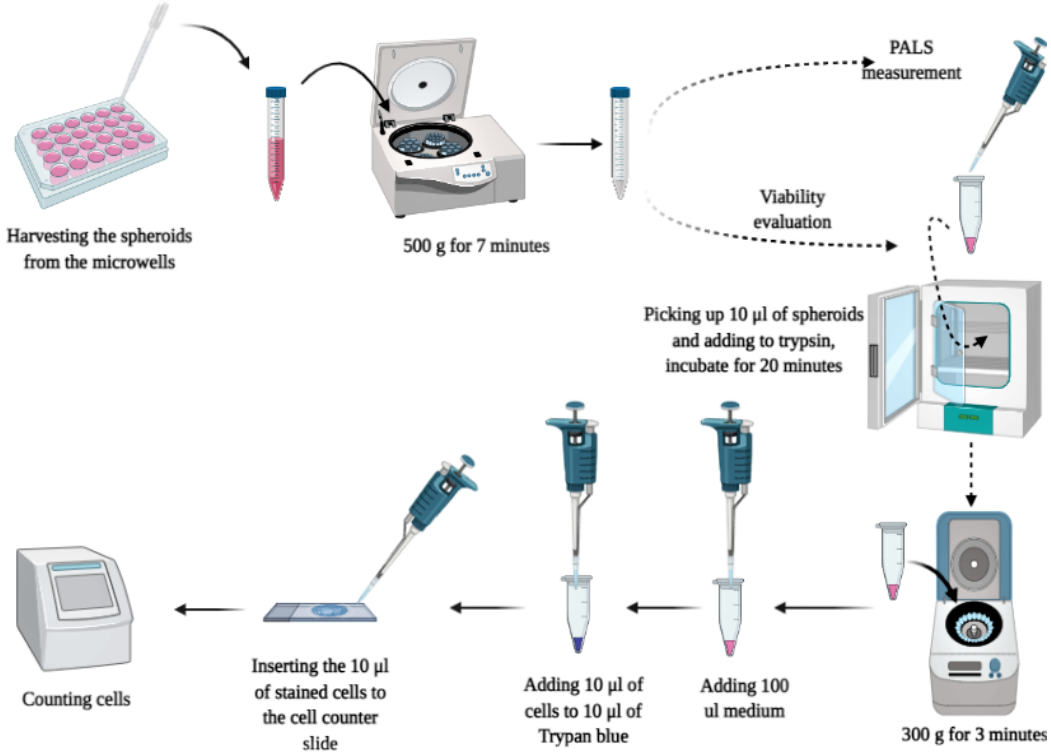

Figure 9.2: Workflow for investigation of spheroid viability after harvesting 3D spheroids from 5D microplates. Figure is created using Biorender.com [30].

9.3 Spectrometer

In this thesis, the positron annihilation lifetime has been evaluated utilizing a PAL spectrometer consisted of two BaF_2 cylindrical detectors (SCIONIX, Holland) connected optically to Hamamatsu photomultipliers with serial numbers SBO696 and SBO697 which were powered by CAEN SY4527 high voltage (HV) power supply. Detectors were connected to a LeCroy 608C constant fraction discriminator (CFD) to receive the coincidence signals. Detectors were set up parallelly (180°) allowing the collection of a satisfactory number of both events, 511 keV and 1274 keV gamma quanta. The 1274 keV gamma quantum comes from deexcitation of ^{22}Ne (START) which is registered by the first

detector and the second gamma quantum with the energy of 511 keV comes from electron-positron annihilation (STOP) which is registered by the second detector, Fig. 9.3.

Furthermore, the source was shifted from the centre axis to the edge of the detectors to provide appropriate geometry and register only pairs of deexcitation and annihilation gamma quanta and prevent registration of two 511 gamma quanta. Positronium lifetime was measured using spectrometer con-

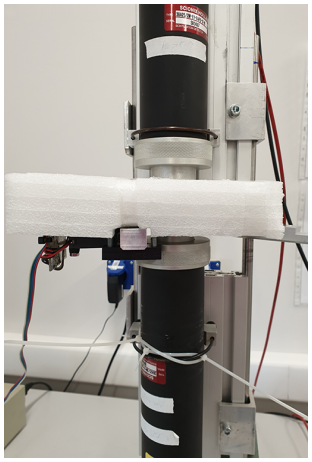

Figure 9.3: Paralleled detectors with cell holder in the middle

sisting of two vertically arranged BaF_2 plastic scintillators (SCIONIX, Holland) and two photomultipliers. A dedicated aluminum chamber was used as a container for spheroids and a holder which was connected to a heater to keep cells at 37^0C. The measurement setup is shown pictorially in Figure 9.4.
^{22}Na radionuclide after emission of positron transforms to the excited state of the ^{22}Ne isotope that deexcites (on the average after 2.6 ps) *via* emission of the 1274 KeV gamma quantum.
Positron loses energy while passing through the cells and eventually annihilates with the electron into two back-to-back 511 keV gamma quanta. The positron-electron annihilation may proceed directly or *via* creation of the positronium. The time between the emission of positron and its annihilation is measured by the registration of the the 1274 KeV deexcitation photon and one of the 511 keV annihilation photons. The sample with the source is positioned in a way (see Fig. 9.4) that enables coincident registration of 1274 keV gamma and one 511 keV photon, and it prevents from the coincident registration of both 511 keV photons flying back-to-back. Before each measurement, the system was calibrated, using an empty chamber including the ^{22}Na source.

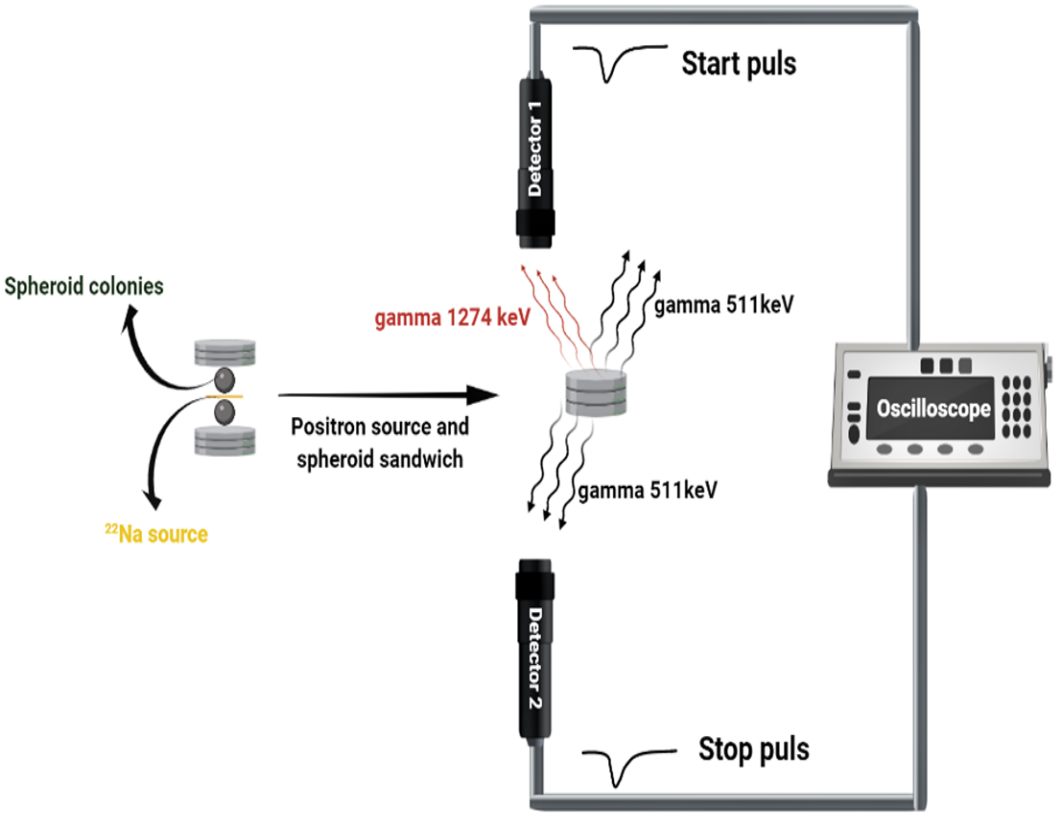

Figure 9.4: Spheroids surrounding the ^{22}Na source are located in the dedicated chamber between two BaF_2 detectors. Spheroids are adjacent to the ^{22}Na source and there is no space or bubble between them. For each measurement 10^6 events with the coincident registration of 511 KeV photon and 1274 keV photon were collected. Figure is created using Biorender.com [30].

9.4 Radioactive source

Positronium is a short-lived hydrogen-like atom consisted of an electron and positron. A positron is an electron-like particle having the same mass but a positive charge. There are different radioactive sources that emit positron such as ^{22}Na presented in Figure 9.5.

In PALS measurement, solid source of $^{22}NaCl$ was used for positron creation. The water solution of $^{22}NaCl$ was dripped on the surface of the thin Kapton foil (6 mm) and let it evaporate. The small drop was evaporated but the small spot of $^{22}NaCl$ crystal (1 mm) with activity of 1 MBq has been remained. Then another thin layer of foil covered the $^{22}NaCl$ crystal and was pressed tightly. This positron source has a lifetime of 2.6 years. The

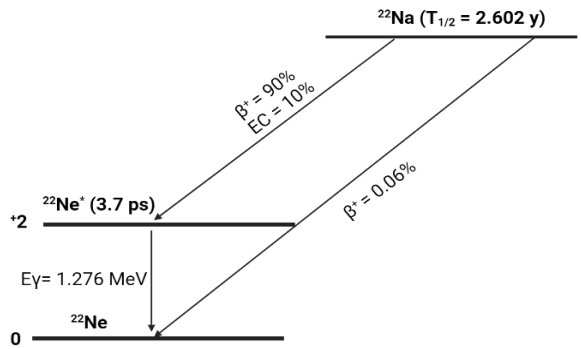

Figure 9.5: Schematic view of ^{22}Na decay

shape of the foils was circle and adjusted to the shape of the chamber used for measurements, Fig 9.6.

When a positron interact with an electron, annihilation happens. ^{22}Na isotope emits gamma quanta with energy of 1274 keV (deexcitation gamma quantum) which is considered as a START signal and the signal from positronium annihilation phenomenon is considered as the STOP signal.

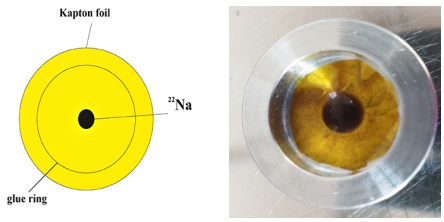

Figure 9.6: Schematic view of ^{22}Na with Kapton foil (left) and ^{22}Na source in the chamber (right).

9.5 Holder and chamber of spheroids

In this thesis, two melanoma spheroids, WM266-4 and WM115, were studied by PALS measurement. The experimental conditions and measurement situation were the same for both samples. The designed chamber for this experiment had a diameter of 0.8 cm and height of 0.4 cm. Chamber was made of aluminium materials, Fig. 9.7.

Since appropriate condition should be provided for cells to maintain them, a viable, chamber for spheroids during PALS measurement required a holder

with temperature control ability to provide the temperature as the same as *in vivo* condition for cells. To measure PALS in 3D spheroids, chamber was placed in the holder and mounted between two detectors, Fig. 9.8.

Figure 9.7: Aluminium chambers for measuring PALS in spheroid samples.

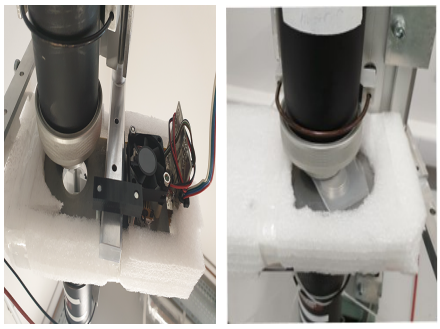

Figure 9.8: Holder of chamber for providing appropriate temperature for cells.

In order to perform the measurement, spheroids were transferred from the centrifuge tube to the chamber by using a scalper and a ^{22}Na radioactive source was placed between the samples. 3D spheroids were placed adjacent to the source, with no air between the source and spheroids. Then the chamber was put inside a holder that was connected to a heater to keep cells at 37^0C. Finally, the holder was located between two BaF_2 detectors, as indicated in Figure 9.4. The lifetime of positronium in 3D spheroids with different ages, 4 and 8 days after seeding cells, has been evaluated based on the 10^6 events collected for each studied case.

9.6 Positron annihilation lifetime spectroscopy in 3D spheroids

In this thesis, it was hypothesized that the difference between the grade of malignancy of the WM115 and WM266-4 melanoma cell lines, present at the level of the cell physiology, are reflected at the nano-molecular level that can be probed by positronium biomarker. Positronium is an exotic atom built of positron and electron. Positronium is formed also in the intra-molecular spaces during the PET diagnosis [17].
In the tissue, positronium may be formed and trapped in the free voids of the intra-molecular spaces, as it is shown pictorially in Figure. 9.9. However, in the intra-molecular voids, o-Ps undergoes processes as pick-off (positron from o-Ps annihilates into two photons (green arrows) with electron from the surrounding molecule) and conversion into p-Ps *via* interaction with molecules as e.g., oxygen molecule. The resulting positronium decays into two photons (brown arrows), Fig 9.9. Therefore, o-Ps lifetime depends strongly on the molecular environment: the nano-molecular structure and concentration of the bio-active molecules [17, 19, 85]. The range of the o-Ps mean lifetime variation is significant, and it changes from the value of 142 ns in vacuum to 1.8 ns in water [86–88]. Properties of positronium in biological samples are only scarcely studied so far. As regards skin cells, they were investigated with low energy positron beam [69, 89–91].
Only recently, the first studies of positronium in the 3D cell structures were performed by culturing cell on collagen matrix [92].

For obtaining reliable and precise results for measuring the positronium lifetime in spheroids, the spheroids without any medium, supernatant, and chemical compounds have been used. In this method, harvested spheroids from the microplates were prepared for positronium lifetime measurement after centrifuge and removing the medium completely from spheroids, Fig 9.2.

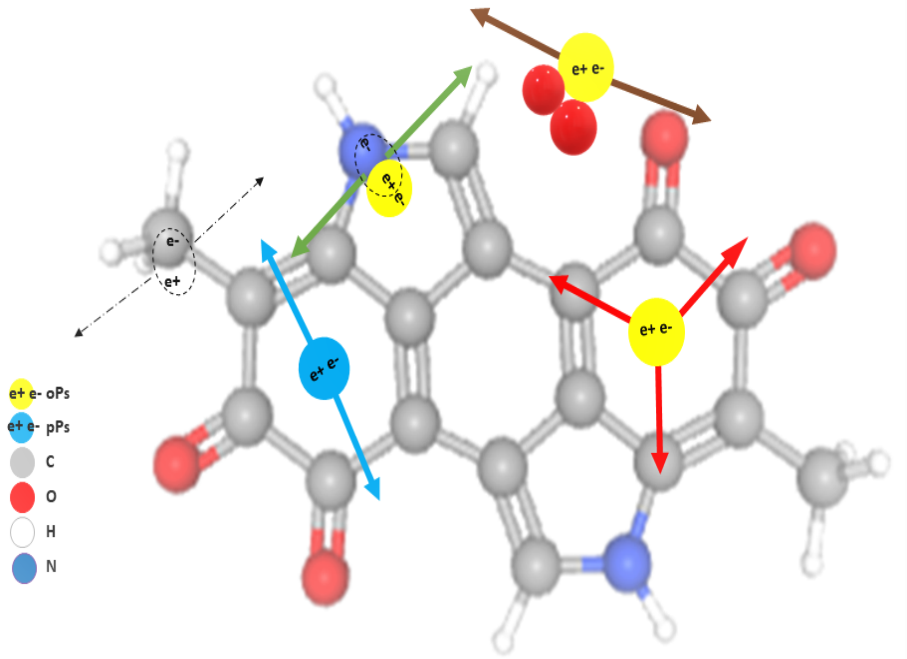

Figure 9.9: Pictorial illustrations of positron annihilations in a melanin molecule. Positron emitted from the radionuclide (eg. ^{18}F in the PET diagnosis or ^{22}Na in the typical PALS experiments) penetrates the object, and after losing the energy annihilates with electron from the molecules constituting the cells. Positron electron annihilation into photons may occur directly (e+e- -> photons (black dashed arrows in Figure 9.9)) or *via* positronium atom (e+e- -> positronium -> photons (solid arrows in Figure 9.9)). In quarter of cases, positronium is formed as short-lived (125 ps) state called p-Ps and in three quarter of cases as long-lived (142 ns) o-Ps. p-Ps (indicated in blue in Figure 9.9) decays predominantly into two photons (blue arrows) and o-Ps decays in vacuum predominantly into three photons (red arrows).

Chapter 10

Data analysis and Image processing

10.1 Statistical analysis

The diameter and growth rate of spheroids was analyzed with ImageJ (v 1.52n) software according to the morphological parameters, circular equivalent diameter, circularity, and roundness (chapter 11.1). Appropriate optical microscopy images were selected to perform this analysis for both melanoma cell lines. To calculate the spheroid diameter, the major and minor axes of a spheroid were considered. The major axis connects to the two farthest points of a spheroid, and the minor axis is considered the shortest line perpendicular to the major axis. This method is also used in the MATLAB image processing toolbox [93]. In this calculation, the cell cloud and debris around the spheroids have not been considered, only solid spheroids with accurate shape and recognized boundaries were evaluated. The significant differences between measurements were calculated using t-test. Statistical analysis was performed by using the OriginPro 2020 software (OriginLab, USA). Tables and graphs include standard deviations or error bars to show the errors from the mean. A value of $P < 0.05$ was considered as statistically significant.

10.2 Bruker software

In micro-CT imaging, captured data was reconstructed and processed with Bruker software (Bruker microCT, Kontich, Belgium) Nrecon (v.1.7.3.1) and CTanalyzer (v. 1.18.8.0+), respectively. An anisotropic diffusion filter was applied to reduce image noise and images were binarized by histogram-based

global thresholding. Afterwards, the 3D watershed separation algorithm was used to separate individual clusters of the spheroid.
In Figure 10.1, histogram presents gray level distribution over whole dataset. Dark gray levels (left side) are the background and image noise (first and second peak). Pink line is a transparency function. It is modified to be flat between 0 and 76, it means this gray level are transparent in the 3D model. The white channel is a light function. It is modified to sigmoidal shape which increases the image contrast. This modifications was applied to the first row in Figure 10.2.

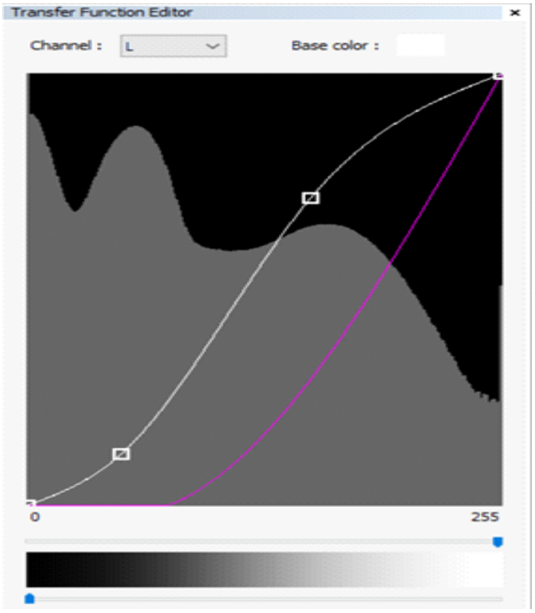

Figure 10.1: Transfer function histogram presents gray level distribution over whole dataset. Dark gray levels are the background and image noise (first and second peak). Pink line shows opacity value and white line presents luminescence.

Images in the second row represent the diameter of the analyzed structure. CTAnalyzer software calculates the diameter of the structure using sphere fitting method, Hildebr-Rüegsegger, and saves images with gray level coded diameter. In CTVox software, the gray level scale can be changed to the color using RGB transfer functions [94]. They assign a color to the particular gray level as in the Figure 10.3.

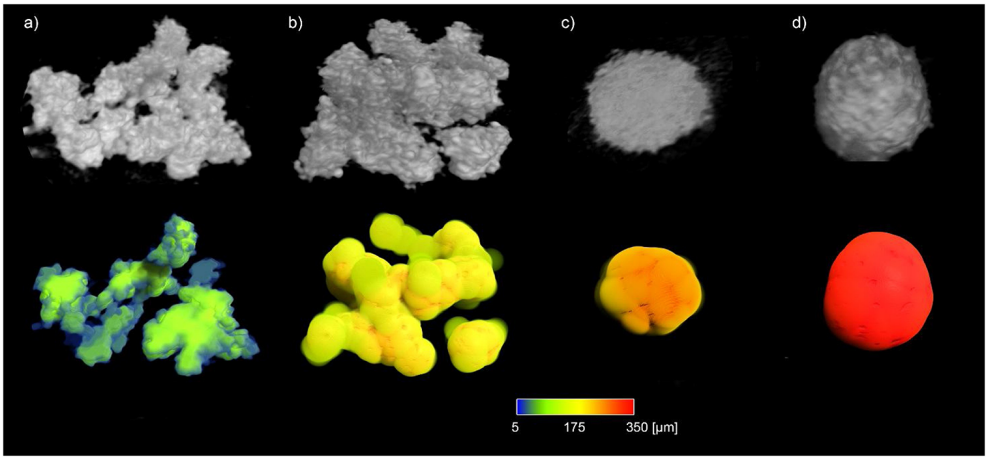

Figure 10.2: Three-dimensional (3D) micro-CT images of melanoma spheroids, WM115 (a,b) and WM266-4 (c,d). Scale indicates the diameter of formed spheroids.

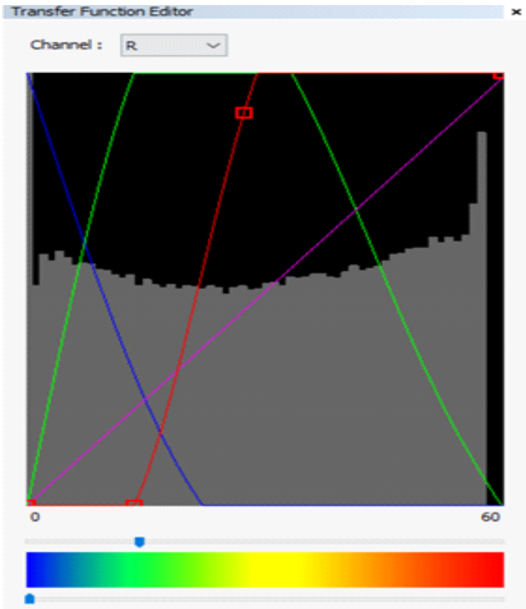

Figure 10.3: In CTVox software the gray level scale can be changed to color using RGB transfer functions. There are 5 values which define the transfer function using not only the colors but also opacity and luminescence. Transfer function changes the gray scale to rainbow. Each line in this graph shows the different color of the rainbow.

10.3 Analysis of positron annihilation lifetime spectra

10.3.1 Charge and Amplitude computation

To register the signals received by two BaF_2 detectors, one oscilloscope has been used during the measurements. Signals which are registered in the oscilloscope channels are voltage dependence and evaluation of signals waveform allows to calculate the charge and amplitude of the signals. Each detector involves a photo-multiplier(PMT), which converts photons into electrical signals. To distinguish the annihilation and deexcitation gamma quantum as well as evaluation of time difference between these two signals, and for the lifetime of positronium, quantification of charge and amplitude is necessary. Figure 10.4 demonstrates the example of a signal which is registered by an oscilloscope [95].

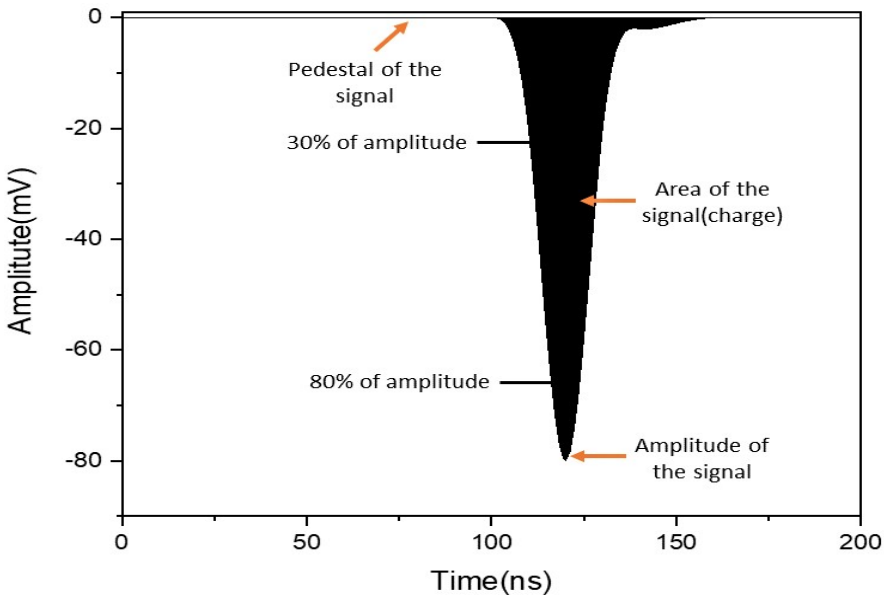

Figure 10.4: Example of collected signal by a digitizer. The black area demonstrates the signal area which is considered as a charge. Pedestal signal is the horizontal line and the amplitude of a signal is estimated as a minimum value of a signal.

The signal pedestal (Ped) has been calculated as the mean of the 10 points of the signal except the first 20 points from the left side of the spectrum.

The signal Pedestal is a required parameter for the charge, amplitude, and

times computations. The minimum value of a signal in the time window has been considered as an Amplitude (A), Eq. 10.1, 10.2. The time difference can be estimated considering the fitted linear function to the leading edge, ranging between 30% to 80% of the amplitude, Fig. 10.4. The time (t) crossing the fitted line is considered on the level of 10% of the amplitude:

$$A = A_{min} - Pedestal, \tag{10.1}$$

$$U_{lin}(t) = at + b, \tag{10.2}$$

where U_{lin} is a fitted voltage at the given time, a and b are the fit values and t is the time. The charge of signal can be estimated by:

$$Q = \int \frac{U(t)dt}{R} \tag{10.3}$$

where U(t) is the voltage and R is resistance which equals to 50Ω in all measurements [95]. The value of $\int U(t)dt$ is calculated as the area under the signal, Fig. 10.4.

The charge of a signal is proportional to the energy deposited in the detector by gamma quantum. Figure 10.5 shows the energy deposition spectrum of ^{22}Na in the detector. As it shows, this spectrum involves four parts based on gamma quanta origination and physical interaction phenomenon in scintilators:

- Photoelectric effect
- Campton scattering

Two parts of the spectrum are dedicated to the photoelectric effect caused *via* both gamma quanta contributes to both photoelectric and Compton effect, two others part of spectrum belongs to Campton Scattering.

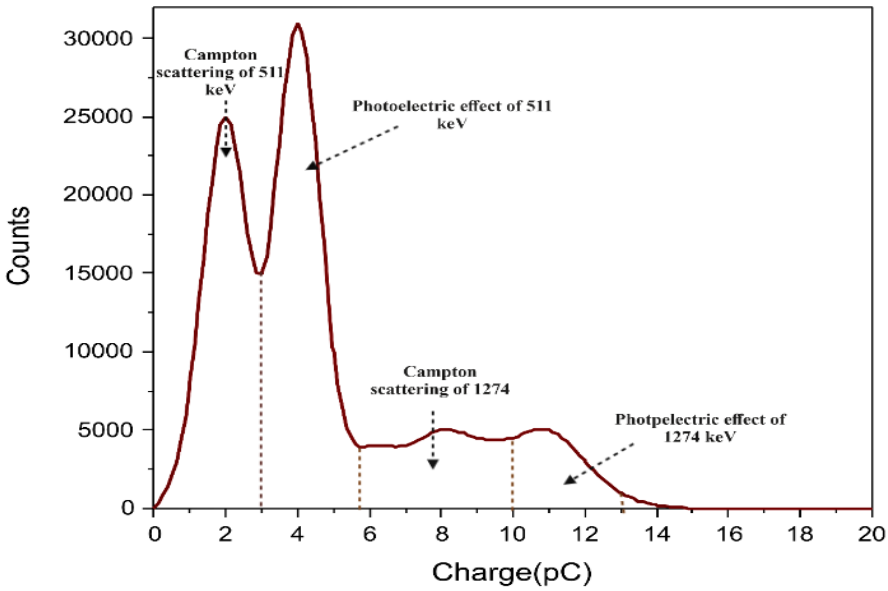

Figure 10.5: Energy spectrum of ^{22}Na with different effects is presented in this figure.

10.3.2 The time difference

The time difference ($\triangle T = T_{511keV} - T_{1274keV}$) of two registered signals can be calculated *via* Eq. 10.2 as a fraction of 10% of the amplitude, Fig. 10.4.

Figure 10.6 indicates example of positron lifetime distribution in linear and logarithmic scale.

10.3.3 Positron lifetime calculation

The positronium lifetime depends on the properties of the material in which it resides. If the matter has a higher density of electrons, then the probability of interaction of the positronium annihilation *via* the pick-off phenomenon is higher leading to shortening the mean lifetime of positronium.

The Positronium lifetime spectrum for one component (τ) can be estimated by Eq. 10.4 [97]:

$$F(\tau, t, \sigma, t_0) = \frac{1}{2 \cdot \tau} exp(\frac{\sigma^2}{2 \cdot \tau^2} - \frac{t - t_0}{\tau})(erf(\frac{t - t_0 - \frac{\sigma^2}{\tau}}{\sqrt{2} \cdot \sigma}) - erf(\frac{-t_0 - \frac{\sigma^2}{\tau}}{\sqrt{2} \cdot \sigma}) \quad (10.4)$$

where erf is an error function (Eq. 10.5):

$$erf(t) = \frac{2}{\sqrt{\pi}} \int_0^x exp(-S^2) ds \quad (10.5)$$

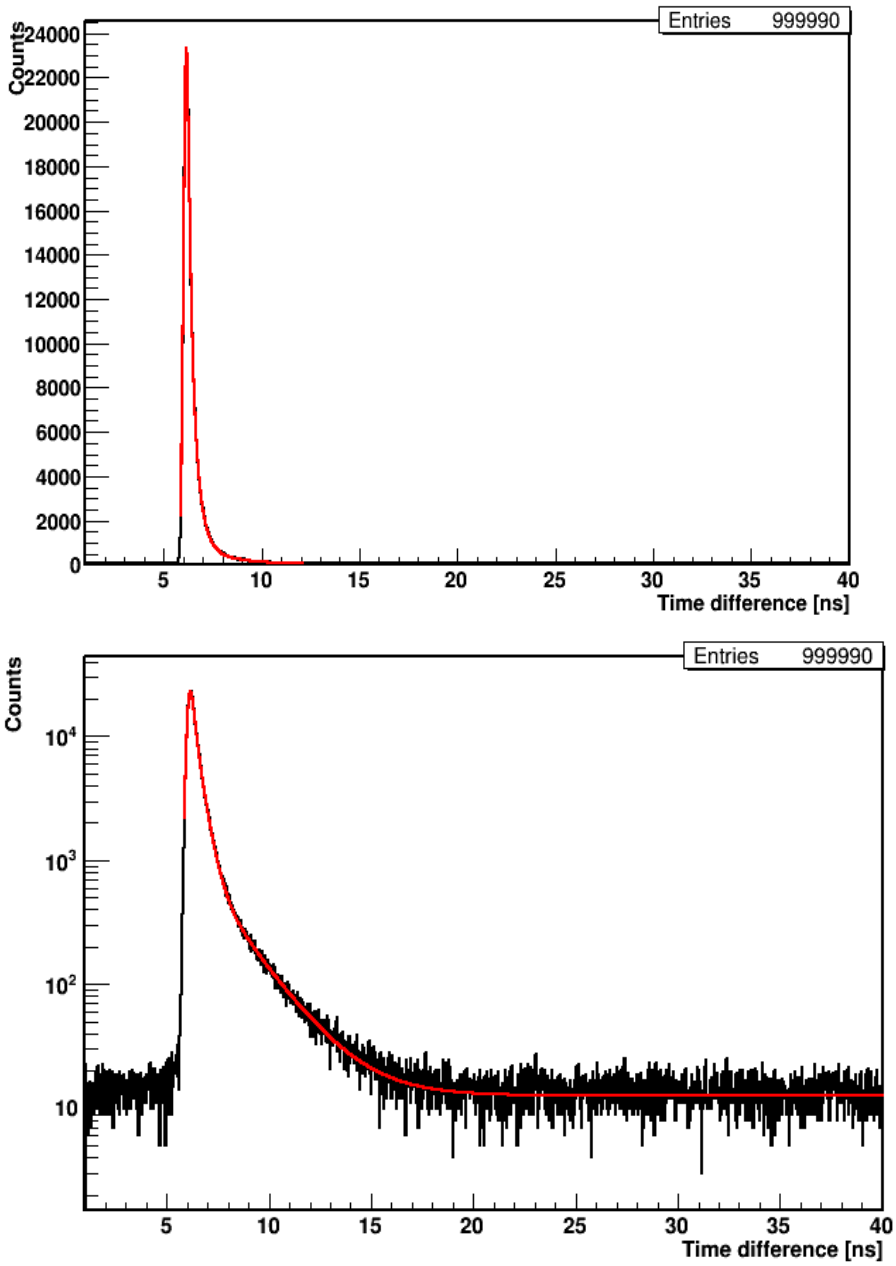

Figure 10.6: Example of lifetime distribution spectra. Red curve shows result of the fit of Eq. 10.6 performed with the PALS Avalanche program [96].

where: τ is the mean lifetime of positron, σ is apparatus resolution, t is the time difference between the registered signals in detectors, and t_0 is offset time of the detector. Positronium lifetime has been analysed using PALS Avalanche program [96–98].

The distribution of mean positronium lifetime between molecules has been calculated by, Eq. 10.6:

$$f(t) = y_0 + \Sigma_{i=1}^{n_\tau} I_i.F(\tau_i, t, \sigma, t_0) \tag{10.6}$$

where: y_0 is considered as the background level, n_τ is the number of components, I_i is the intensity of ith component and τ_i is the mean lifetime of the ith component.
In this Ph.D thesis, four components (n_τ= 4) have been considered in spectra regarding the lifetime and intensity, Table. 10.1. The exemplary spectrum with the result of the fit is shown in Figure 10.7.

Lifetime	Intensity	type of component
τ_1	I_1	p-Ps annihilation
τ_2	I_2	free positron annihilation in the sample
τ_s	I_s	free positron annihilation in the source
τ_3	I_3	o-Ps annihilation

Table 10.1: The different positron annihilation processes in the material

10.3.4 Gain callibration

In engineering, the gain is a parameter controlling the ability of an amplifier, to increase the power of an electric signal as a function of voltage. Owing to the dependency of positronium lifetime on the time and energy resolution, gain calibration for PMTs has been applied. Figure 10.8 shows the photomultiplier tube construction. A photomultiplier is consisted of :

- evacuated glass tube which other parts are placed in this tube
- input window
- a photocathode
- focusing electrodes
- an electron multiplier
- an anode

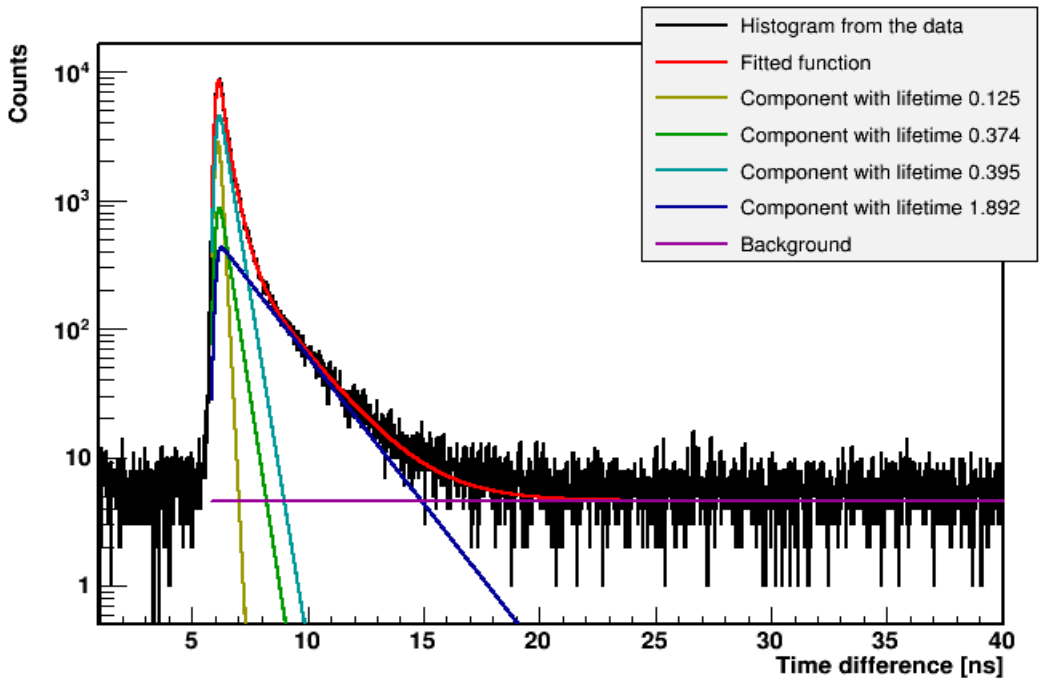

Figure 10.7: Exemplary experimental lifetime spectrum (black histogram) with superimposed histograms resulting from the fit of the sum of the exponential function convoluted with the detector resolution (Eq. 10.6), performed by means of the PALS Avalanche program [96, 99]. First component (yellow line) shows the contribution from p-Ps (mean lifetime: 0.1 - 0.2 ns), second component (green line) originates from annihilations in source (Kapton foil) (0.37 ns), third component (light blue) shows free annihilation lifetime in the source (0.2 - 0.6 ns), forth component (dark blue) illustrates the contribution from o-Ps. A sum of all contributions resulting from the fit is shown as a red curve.

When a photon enters the PMT tube, it can be detected and registered through the following processes:

1. Photons enter the evacuated glass tube *via* input window and hits the photocathode;

2. Photons excite the photocathode electrons and release the photoelectrons into the vaccume tube;

3. Photoelectrons are accelerated due to the electric field and hit the first dynode.

4. After hitting the dynode, the photoelectrons are multiplied and lead to

secondary electron emissions. The secondary emission is repeated at all dynodes

5. At last, secondary electrons emitting from the last dynode will be collected at anode.

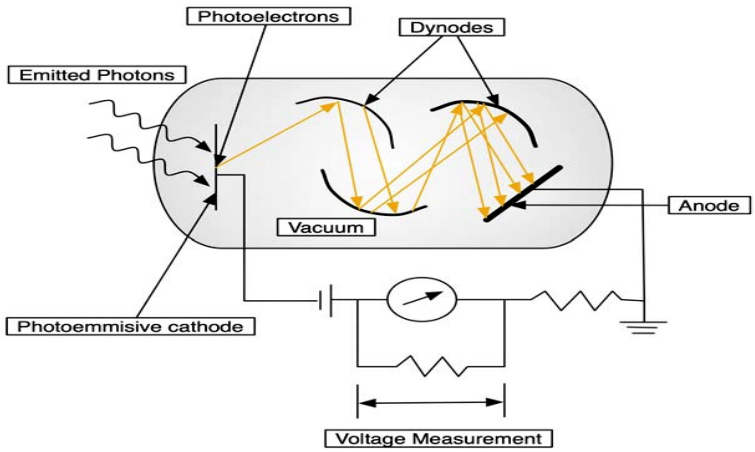

Figure 10.8: Schematic view of the electron emission in a photomultiplier tube adopted from JR. Quinn et al [100]. Due to the photoelectric effect, the photocathode emits photoelectrons after the collision of photons with the photocathode. According to the voltage, each dynode amplifies the number of electrons. Therefore with the collision of a huge number of electrons with dynodes, the current is generated.

As a consequence, the number of dynodes and secondary emission coefficient has an important influence on PMTs gain. Where μ is gain which describes amplification of single electron, secondary emission coefficient is δ, n is the number of dynodes, K is constant, U is applied electric field between two dynodes and α is the coefficient defined by the geometry and dynode material, Eq. 10.7 [101]:

$$\mu = \delta^n = K \cdot U^{n.\alpha} \tag{10.7}$$

Regarding Eq. 10.8, the gain dependency on the voltage supplied to the photomultiplier can be formulated *via*:

$$\mu(U) = a \cdot U^b \tag{10.8}$$

Where a and b are the fit parameters.

Part III

Results

Chapter 11

Determination of Spheroid characteristics using biochemical and imaging techniques

11.1 The rate of growth and shape analysis

The spheroid size depends on the initial number of cells seeded at the start of culture and significantly increases along with the time of culture. Figure 11.1 demonstrates how WM115(a) and WM266-4(b) spheroids with different initial cell seeding were growing during the time. WM266-4 spheroids had significantly higher mean diameter for all initial cell seeding, 500 cells ($p = 0.0003$), 1000 and 1500 ($p < 0.001$) than WM115 spheroids, which is related to their malignancy characteristics, Tab. 11.1 and 11.2. Over one week, WM266-4 spheroids showed a clear increase in both circularity and roundness for all initial cell densities, Fig 11.2. While both spheroids become rounder and more circular during the time, WM266-4 spheroids had more circularity than WM115 spheroids ($p < 0.001$) over the one week culturing, Tab. 11. and 11.2

WM266-4 and WM115 spheroids roundness was gradually increasing, and there were no difference between WM266-4 and WM115 cell lines for 500 ($p = 0.16$), 1000 ($p = 0.1$) and 1500 ($p = 0.09$) spheroids. The statistically significant difference between WM266-4 and WM115 spheroids was calculated at day 7th for all initial cell seeding to show how WM266-4 and WM115 spheroids have been changed after one week growth.

The volume (V) of each spheroid was calculated according to the (Eq. 11.1):

$$V = \frac{4}{3}\pi r^3 \tag{11.1}$$

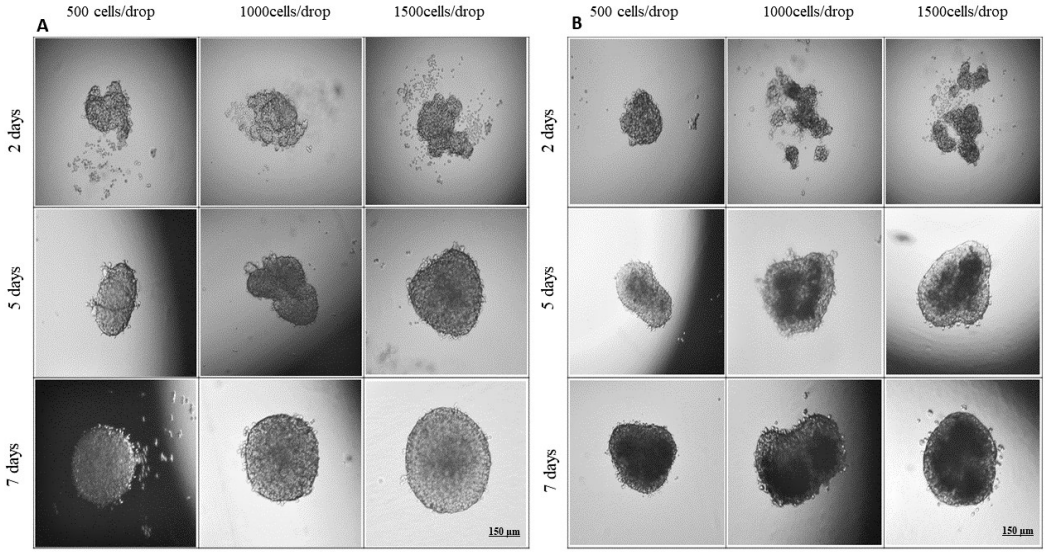

Figure 11.1: Optical microscopy images of spheroid melanoma WM266-4 (A) and WM115 (B), demonstrate how spheroids are growing during the culturing time. Both spheroids are generated using hanging drop method with 500, 1000, and 1500 cells/drop. Over the time, spheroids grow and show enlargement in their size and more circularity and roundness in their shape [79].

where r is the radius of a spheroid. The growth rate of spheroids has been calculated *via* equation 11.2 [102, 103]:

$$log\frac{V_2}{V_1} = k(t_2 - t_1) \tag{11.2}$$

where V_2 is the spheroid volume at time t_2 and V_1 is the spheroid volume at time t_1 and k is the rate of growth.
WM266-4 and WM115 spheroids with 500 initial cells exhibit the growth rate (k) of 1.03 μm^3/day and 1.02 μm^3/day during a week, respectively. WM266-4 and WM115 spheroids formed from 1000 cells demonstrate a growth rate of 1.07 μm^3/day and 1.04 μm^3/day and spheroids with 1500 initial cells show 1.1 μm^3/day and 1.07 growth rate during the culturing time, respectively.

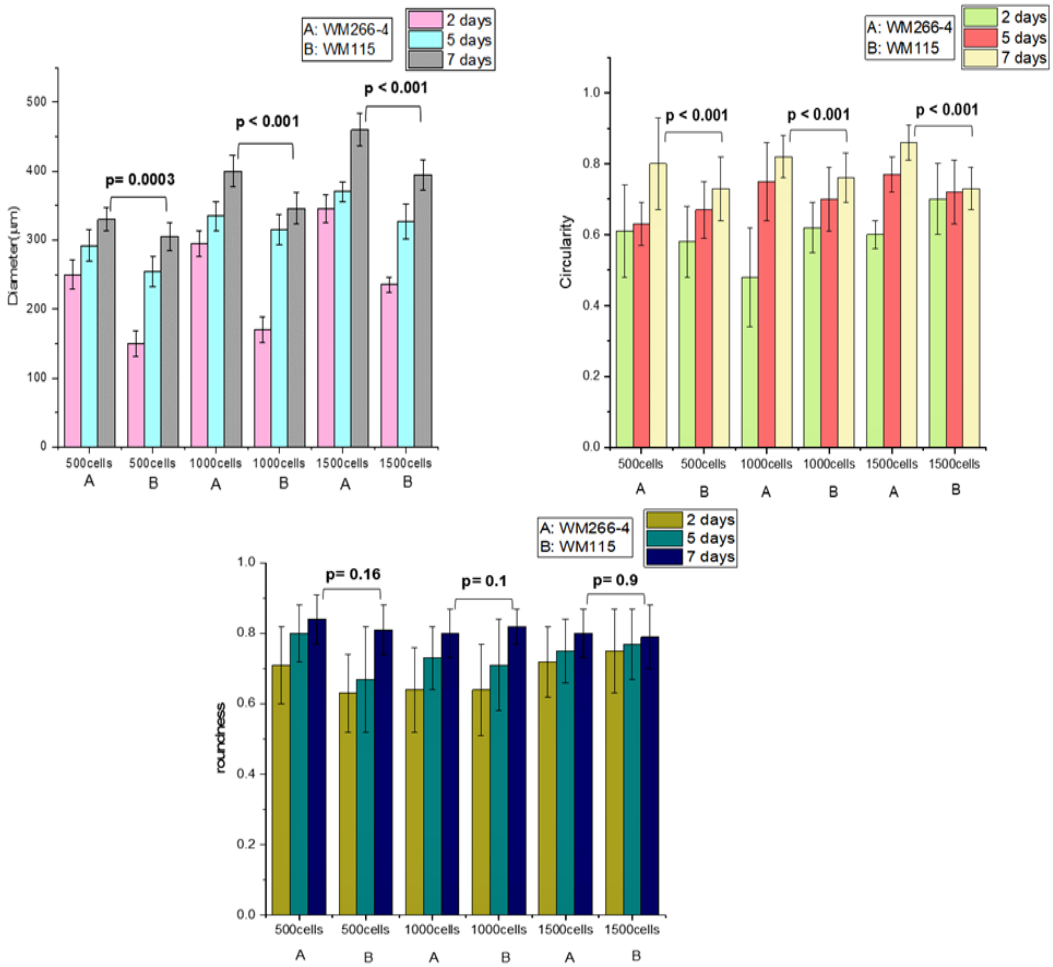

Figure 11.2: The diameter, circularity and roundness of spheroids formed by melanoma cell lines, WM266-4 and WM115, have been changed during the time. WM266-4 spheroids show a more regular increase in circularity while WM115 spheroids illustrates the semi-regular increase in circularity. The statistically significant difference between WM266-4 and WM115 spheroids has been compared at the day 7th.

Initial cell number[n]	day	Diameter(μm)(SD)	Circularity(SD)	Roundness(SD)
500	2	250(21)	0.61(0.13)	0.71(0.11)
500	5	292(23)	0.63(0.06)	0.8(0.08)
500	7	330(17)	0.8(0.13)	0.84(0.07)
1000	2	295(19)	0.48(0.14)	0.64(0.12)
1000	5	335(21)	0.75(0.11)	0.73(0.09)
1000	7	400(23)	0.82(0.06)	0.8(0.07)
1500	2	345(20)	0.6(0.04)	0.72(0.1)
1500	5	370(14)	0.77(0.05)	0.75(0.09)
1500	7	460(23)	0.86(0.05)	0.8(0.07)

Table 11.1: Mean diameter, circularity and roundness of WM266-4 spheroids with different initial cell number during culturing time.

Initial cell number[n]	day	Diameter(μm)(SD)	Circularity(SD)	Roundness(SD)
500	2	150(19)	0.58(0.1)	0.63(0.11)
500	5	255(22)	0.67(0.08)	0.67(0.15)
500	7	305(21)	0.73(0.09)	0.81(0.07)
1000	2	170(19)	0.62(0.07)	0.64(0.13)
1000	5	315(22)	0.70(0.09)	0.71(0.13)
1000	7	346(23)	0.76(0.07)	0.82(0.05)
1500	2	235(11)	0.70(0.1)	0.75(0.12)
1500	5	327(25)	0.72(0.09)	0.77(0.1)
1500	7	395(22)	0.73(0.06)	0.79(0.09)

Table 11.2: Mean diameter, circularity and roundness of WM115 spheroids with different initial cell number during culturing time. SD= standard deviation

11.2 Viability

The viability of cells in a single spheroid was evaluated at 5th and 7th days after cell seeding. The viability of spheroids was classified by fluorescence microscopy: green fluorescence indicated viable cells and red indicated dead cells. Viable cells were found mostly on the surface and the edge of the spheroid that is well known as proliferation zone. Most of the cells in this layer were alive and proliferate appropriately, whereas dead cells were located predominantly in the center of the spheroid or necrotic core where cells encounter to lack of essential nutrients for growth, Tab 11.3, 11.4.

Figure 11.3 demonstrates how a spheroid grew and cells were proliferating. As a spheroid grows, the number of cells increases and the competition for essential nutrients arise, therefore the central cells become death due to the nutrients restriction [79].

In this experiment, the number of cells in spheroids with different initial cell seeding has been calculated *via* Eq. 11.3, 11.4:

$$N = N_0 e^{k(t-t_0)} \tag{11.3}$$

$$k = \frac{ln2}{DT} \tag{11.4}$$

where N is the number of cells at time t and N_0 is the number of cells at t_0. The doubling time(DT) of spheroids is usually characterized like real tumor doubling time and is calculated by using spheroid volume *via* Eq. 11.5 :

$$DT = \frac{t \cdot ln2}{ln\frac{V_2}{V_1}} \tag{11.5}$$

Where V is spheroid volume and t is the time of culturing. [104, 105].

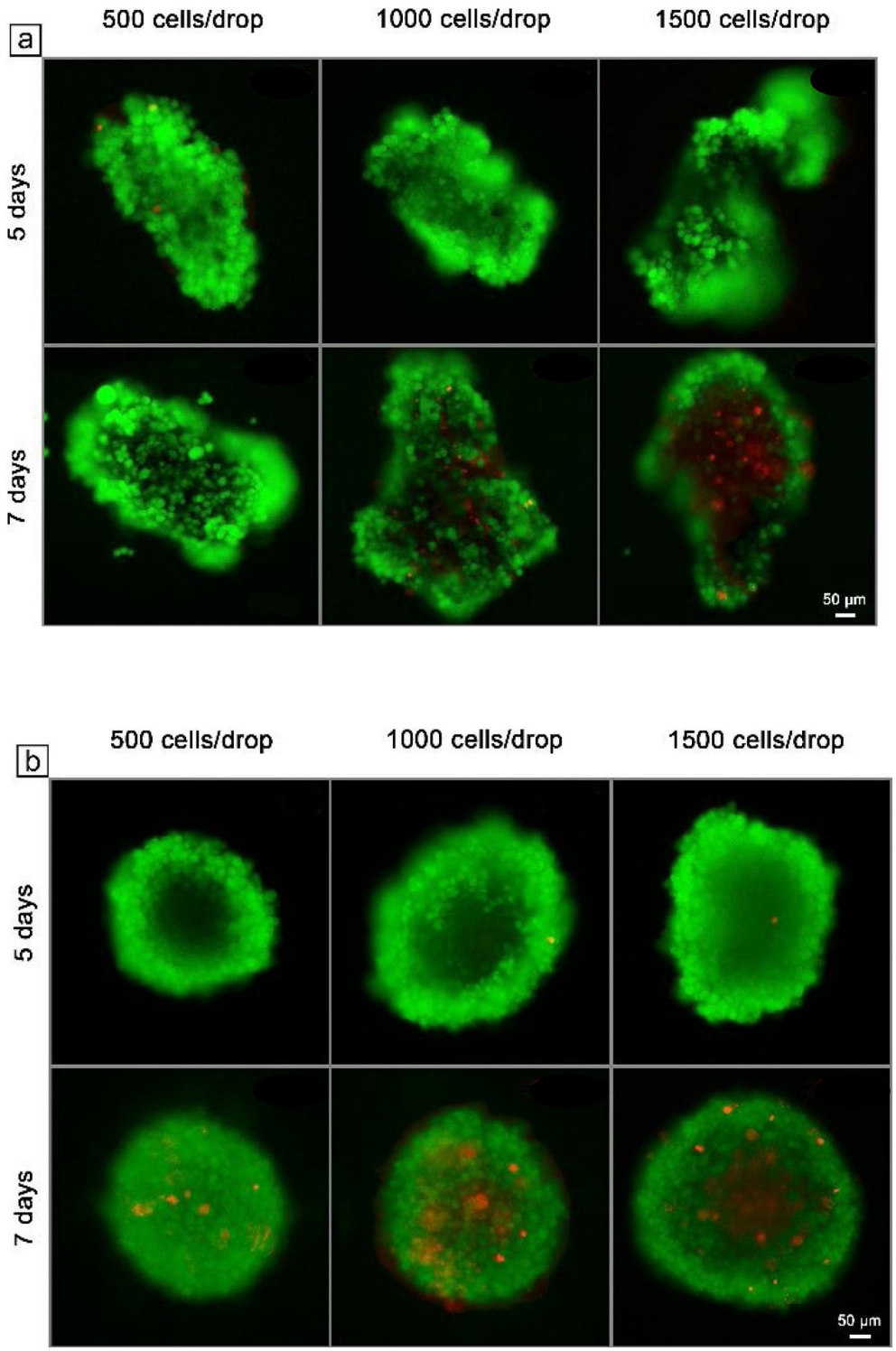

Figure 11.3: Fluorescence images of WM115(a) and WM266-4(b) spheroids have been taken 5 and 7 days after cell seeding.

Initial cell number[n]	day	alive cells(percentage)	dead cells(percentage)
500	5	1579(98.2%)	28(1.8%)
500	7	2501(99.9%)	1(0.04%)
1000	5	3150(99.8%)	4(0.15%)
1000	7	4522(93.93%)	274(6.07%)
1500	5	4725(99.9%)	1(0.04%)
1500	7	7500(70.64%)	2202(29.36%)

Table 11.3: The number of alive and dead cells in WM115 spheroids with different initial number of cells in two culturing time.

Initial cell nimber[n]	day	alive cells(percentage)	dead cells(percentage)
500	5	1820(100%)	0%
500	7	3085(93.58%)	198(6.42%)
1000	5	3660(99.7%)	10(0.28%)
1000	7	6171(72.84%)	1674(27.16%)
1500	5	5690(99.5%)	27(0.49%)
1500	7	9255(86.34%)	777(13.66%)

Table 11.4: The number of alive and dead cells in WM266-4 spheroids with different initial number of cells in two culturing time.

11.3 Microtomography imaging

Optimization of micro-CT procedure proved challenging as the results were highly variable, demonstrating sensitivity to even subtle changes in the contrasting and fixation protocols. The spheroids were found to be highly sensitive to some of the staining and/or fixation methods used, which can cause deformation or even death of the spheroids. The most suitable image was obtained after staining for 1.5 h with Lugol solution, without fixation.

After applying a combination of image denoising and Otsu thresholding, it was possible to perform a 3D watershed separation to analyze individual spheroid and final visualizations of spheroids were obtained using volume rendering in CTVox software (v. 3.3.0 r.1403, Bruker micro-CT, Kontich, Belgium). Spheroids from both cell lines grew and, over time, developed into more dense structures. However, WM266-4 cells produced a single, well-defined spheroid with a smooth surface, while WM115 cells were scattered and produced clusters of low-diameter spheroids instead.

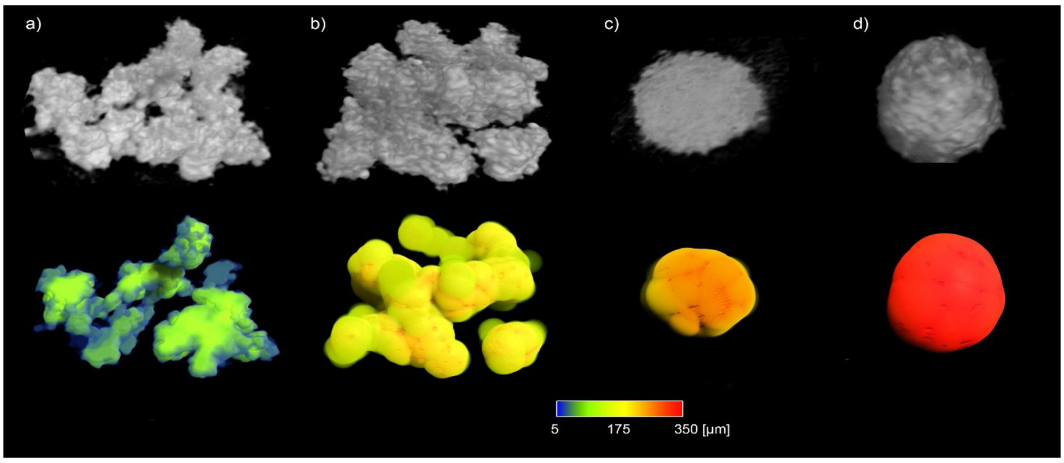

Figure 11.4: Three-dimensional(3D) micro-CT images of spheroids formed by WM115 cells after 5 days (a), 7 days (b) and WM266-4 cells after 5 days (c), 7 days (d). Scale indicates the diameter of formed spheroids [79].

Chapter 12

Determination of nutrient diffusion in spheroids using bioluminescence techniques

12.1 2-NBDG uptake monitoring in 3D melanoma spheroids using confocal microscopy

In this thesis, 2-NBDG that can enter both malignant and non-malignant cancer cells, have been considered as an appropriate probe to determine the rate of glucose uptake in two different melanoma spheroids, WM266-4, and WM115, Fig 12.1. Figure 12.2 illustrates how fluorescence intensity is changing regarding the distance from the surface of a spheroid, the number of cells, culturing time, and malignancy level. WM266-4 spheroids with malignancy characteristics demonstrated higher uptake of glucose than non-malignant melanoma spheroids, WM155. As mentioned before, each 3D spheroid has a multi-layer structure; therefore, as moving from the surface of a spheroid to the center of the spheroid, the fraction of proliferating cells decreases, and the quiescent layer with live cells but not proliferation ability and hypoxia region will appear. The glucose and oxygen concentration in spheroids have been calculated *via* Fick's law equation 12.1 and 12.2 :

$$\frac{1}{r^2}\frac{d}{dr}(N_i)(r^2) = P_i \tag{12.1}$$

$$-D_i\frac{dC_i}{dr} = N_i \tag{12.2}$$

Where r is spheroid radius, N_i is molar flux of the components(glucose or oxygen) and P_i is the rate of concentration of the component, C_i is extracellular concentration of component and D_i is the effective diffusion coefficient [106, 107].

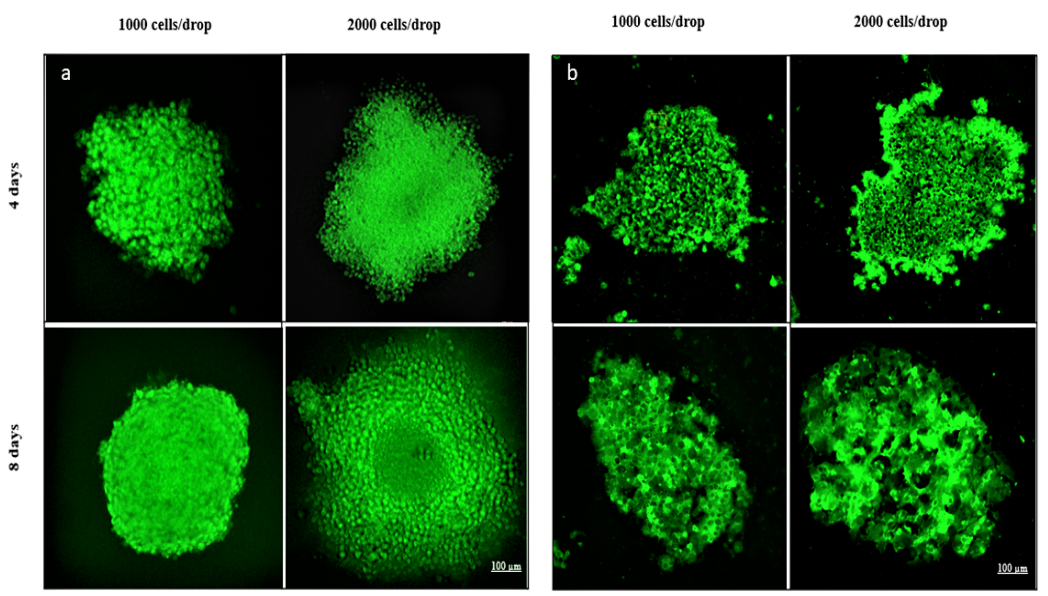

Figure 12.1: Confocal microscopy images of WM266-4 (a) and WM115 (b) melanoma spheroids for showing glucose distribution.

By calculating the volume of spheroids and the concentration of D-glucose molecule in medium, for *in vitro* study, the rate of glucose concentration can be estimated *via* Eq. 12.1, 12.2. According to the fluorescence intensity analysis, Fig. 12.2, 100 to 200 μm of outer layer of a spheroid was considered as the proliferation rim, and 50-100 μm of inner part of the spheroid was considered as necrotic core. However, the size of different layers of a spheroid depends on the size of the spheroid. The glucose concentration in the proliferation layer of WM266-4 and WM115 spheroids was higher; 78 μM and 59 μM, respectively. Although it was decreasing in the innermost layer of WM266-4 and WM115 spheroids owing to the emersion of the necrotic core, 1.4 μM and 4.1 μM, respectively. By moving towards the center of a spheroid, glucose concentration decreased gradually, Fig 12.3. It should be noted that this amount of glucose concentration has been calculated for proliferation rim and necrotic region only not entire spheroid to show the different glucose uptake rate in different layers

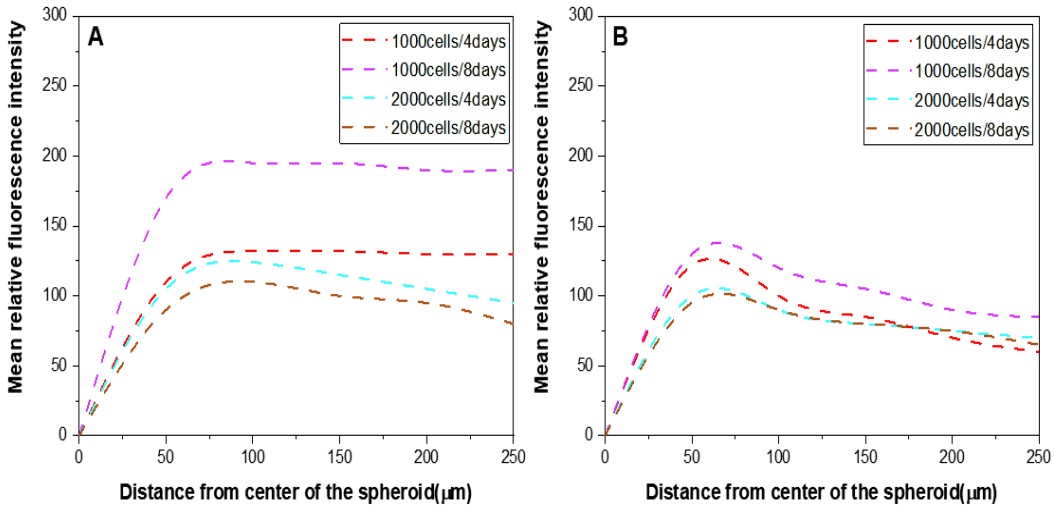

Figure 12.2: Glucose distribution assay has been done by 2-NBDG probe in WM266-4(A) and WM115(B) melanoma spheroids.

of a spheroid. The rate of glucose concentration vary from 0.1 to 0.4 mM in real solid tumors in comparison to an average blood glucose concentration of 4 to 7 mM [108, 109]. The rate of glucose concentration in real tumors depends on the size of tumor, location and the stage of cancer cells. In contrary, the rate of glucose concentration in spheroids is lower than real tumor studies due to their small size, volume and *in virto* condition.

Regarding the fluorescence intensity in both kind of spheroids with 1000 initial number of cells after 4 days, glucose uptake intensity in proliferation rim of WM266-4 spheroids was not significantly higher than WM115 spheroids($p = 0.20$) while in the deeper region, WM266-4 spheroids showed higher glucose uptake intensity($p = 0.00001$) than WM115 spheroids. On day 8, WM266-4 spheroids showed higher glucose uptake intensity($p = 0.001$) than WM115 spheroids in both proliferation rim and deeper layer. In bigger spheroids with 2000 initial cell numbers after 4 days, the glucose uptake intensity was significantly higher in proliferation rim($p = 0.04$) and depth ($p = 0.0018$) of WM266-4 spheroids with respect to WM115 spheroids. On day 8, WM266-4 and WM115 spheroids exhibited a significant difference in glucose uptake intensity in the outer layer($p = 0.007$) but not in the inner part($p = 0.064$). The glucose concentration in the outer rim of WM266-4 spheroids was higher with respect to WM115 one.

Figure 12.3 illustrates how fluorescence intensity is changing regarding the distance from the surface of a spheroid, the number of cells, culturing time, and

malignancy level. WM266-4 spheroids with malignancy characteristics demonstrated higher uptake of glucose than non-malignant melanoma spheroids, WM155.

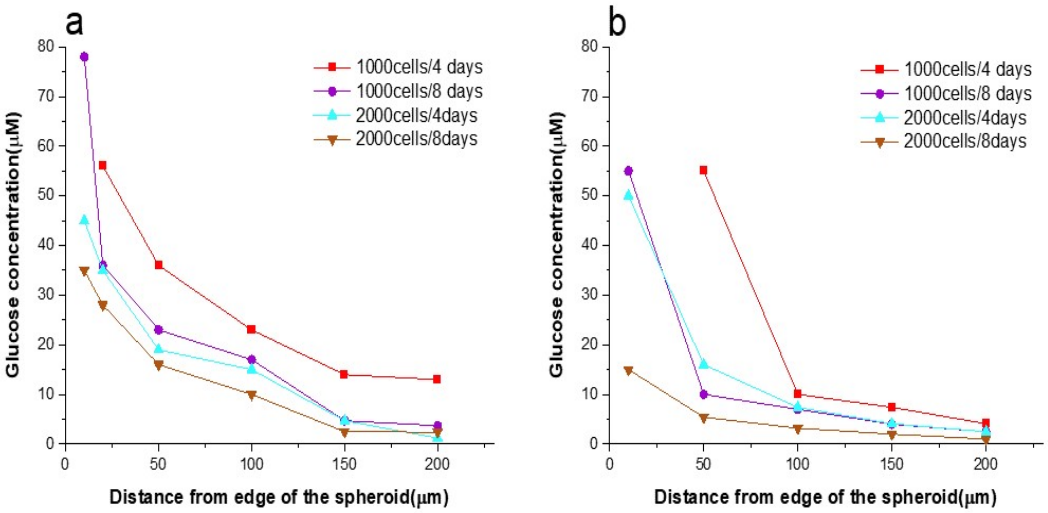

Figure 12.3: Graph of glucose concentration in WM266-4(a) and WM115(b) melanoma spheroids.

12.2 Determination of a hypoxic region

In this thesis, two types of spheroid with a difference in size, culturing time, and malignancy level have been compared. The results show that by moving through the center of a spheroid, the oxygen concentration decreases significantly. Figure 12.4 demonstrates the confocal microscopy images of oxygen distribution in WM266-4 and WM115 spheroids. Regarding the rate of fluorescence intensity in both spheroids with 1000 initial number of cells after 4 days, hypoxia progression in WM266-4 spheroids was not significantly higher than WM115 spheroids ($p > 0.05$) while at day 8 the degree of hypoxia in the center of WM266-4 spheroids was significantly higher than WM115 spheroids ($p = 0.0001$). In bigger spheroids with 2000 initial cells at the time of culturing, the degree of hypoxia in WM266-4 spheroids was significantly higher ($p < 0.001$) than WM115 spheroids while at day 8, WM266-4 and WM115 spheroids exhibited a significant difference in hypoxia progression in their center ($p = 0.00048$) but not in the outer part ($p = 0.24$). Figure 12.5 shows the hypoxia progression in two melanoma spheroids. It is visible that hypoxia in WM266-4 and WM115 spheroids is increasing by moving towards the center of a spheroid.

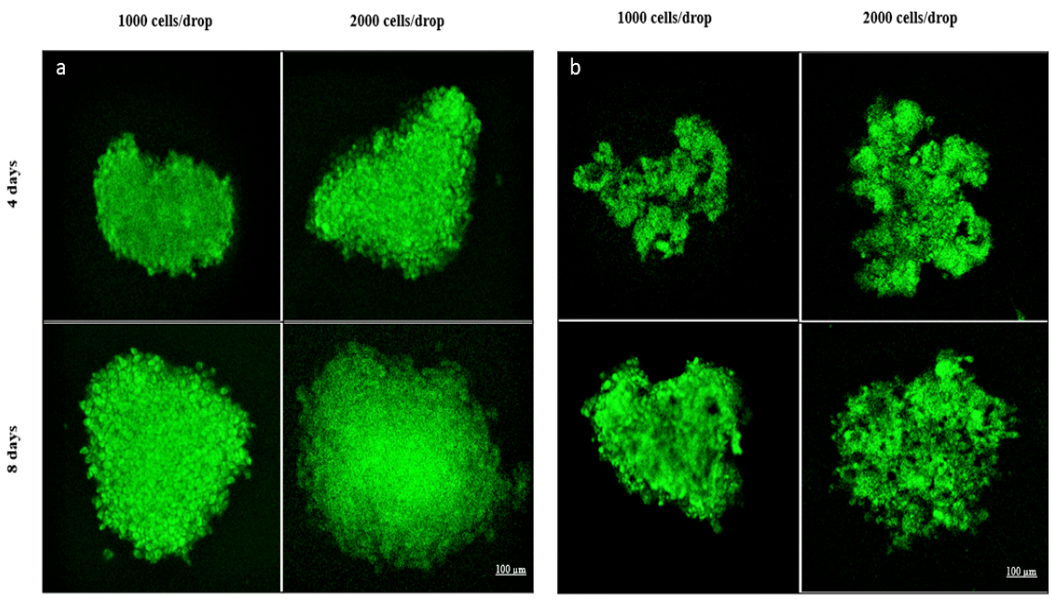

Figure 12.4: Confocal microscopy images of melanoma spheroid cell lines; WM266-4 (a), WM115 (b) for showing the hypoxia region.

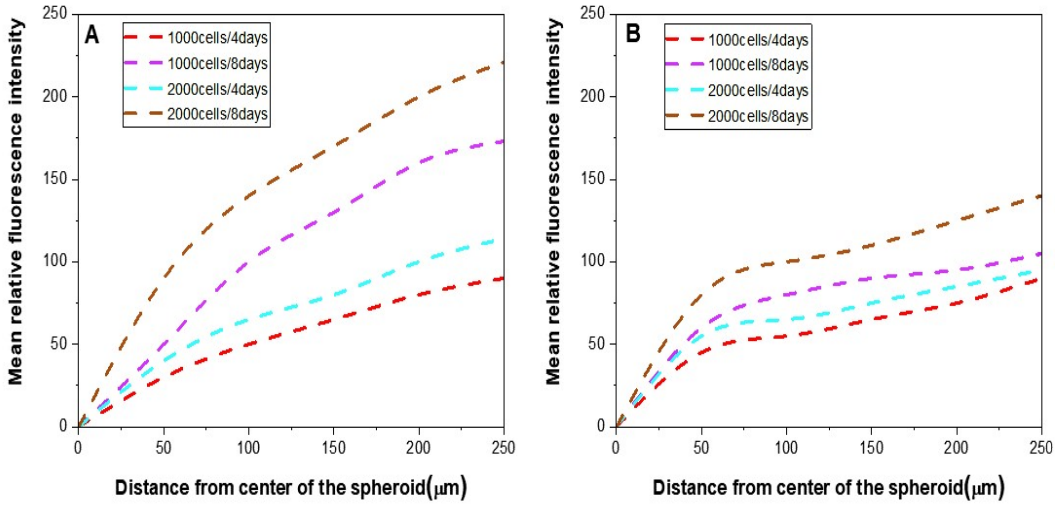

Figure 12.5: Graph of hypoxia distribution in WM266-4(A) and WM115(B) spheroids in two different culturing time has been evaluated using Image-IT™ Green Hypoxia probe.

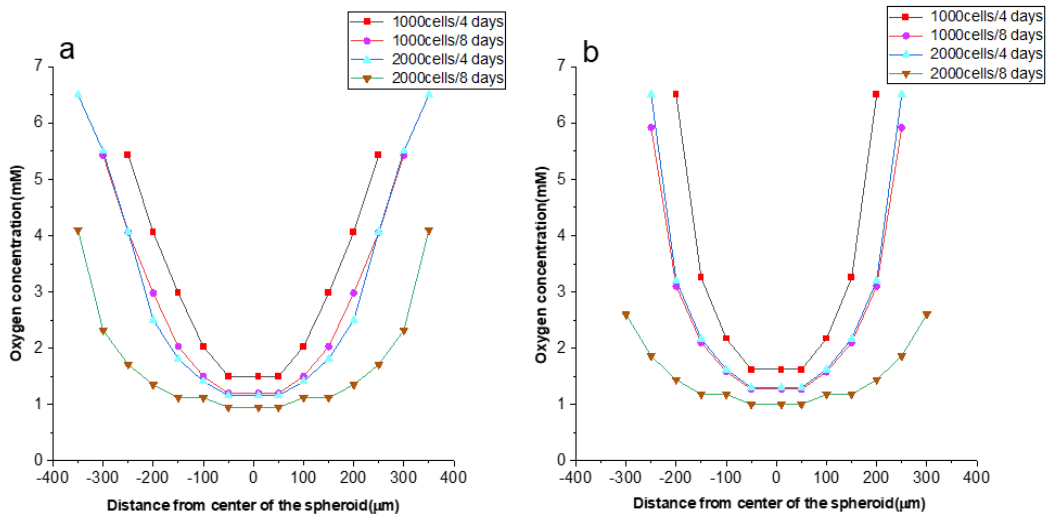

Figure 12.6: Oxygen concentration in WM266-4(a) and WM115(b) spheroids. As spheroids grow in diameter, the rate of oxygen uptake in inner layers of a spheroid decrease gradually and leads to appearance of hypoxia region and necrotic core.

During the culturing time, the spheroid grows and the diameter of the spheroid increases gradually; therefore, the propagation of oxygen to the center of the spheroid will be reduced due to the bigger size and larger number of cells.

The oxygen concentration in a single spheroid has been calculated *via* mathematical modeling, equations 12.1, and 12.2.
Results showed the oxygen concentration in the proliferation layer of WM266-4 and WM115 spheroids was higher; 6.5 mM. However, it was decreasing by moving towards the center of the spheroid, 0.95 mM and 1.002 mM for WM266-4 and WM115 spheroids, respectively, Fig 12.6.
The oxygen level in normoxia condition is 21% (160 mmHg). The oxygen level in normal tissue is typically lower in the range of 3 - 9%(22 - 68.5 mmHg). The oxygen concentration in tumors is much lower around 0.3 - 5% [110, 111]. The results show the rat of oxygen concentration in WM266-4 and WM115 spheroids is around 3% (22 mmHg) in proliferation rim and 0.05% and 0.006% in the center of spheroids, respectively which follows the the oxygen level in real tumors.

Chapter 13

Determination of positronium lifetime in melanoma spheroids with different malignancy level

13.1 Spheroid morphology and proliferation rate

Figure 13.1 shows the spherical structure of spheroids in the micro plate which was expected. WM266-4 cell lines formed more spherical and concentrated spheroids in comparison to WM115 cell line. Spheroids in both cell lines showed an increase in their size and circularity over the time. Figure 13.2 presents, that there is an increase in the number of cells and volume of both spheroids from cell seeding until the 8th day after culturing. For WM266-4, it results in 1.5 and 2.74-fold increase of cell number after 4th and 8th day, respectively. Number of cells in WM115 spheroids increased 1.4 and 1.7-fold after 4 and 8 days, respectively. WM266-4 spheroids showed more proliferation than WM115 spheroids, however there was no significant difference between WM266-4 and WM115 spheroids after 4 days of culturing($p = 0.55$), but the number of cells in WM266-4 spheroids was significantly different($p = 0.028$) than WM115 spheroids after 8 days, Fig 13.2. In each positronium lifetime measurement, a total of 36000 spheroids were used.

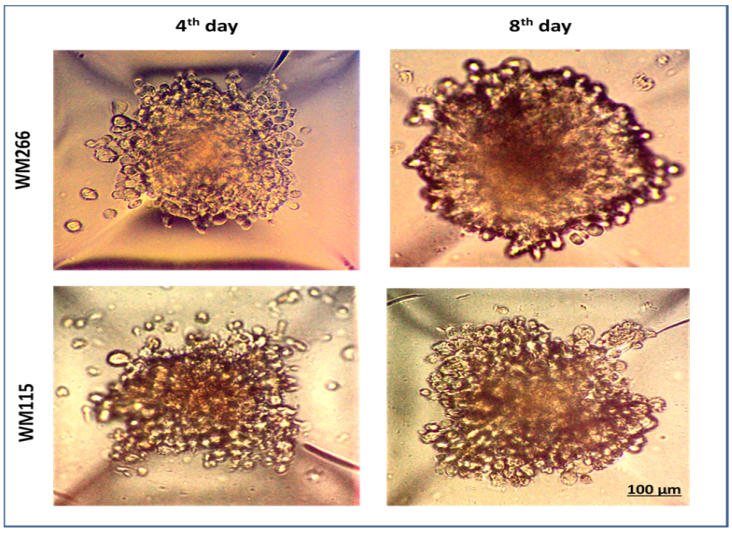

Figure 13.1: Microscopic images of two different melanoma cell lines, WM266-4 and WM115, the 4th and 8th day of culturing. The density and circularity of spheroids is increasing during the culturing time.

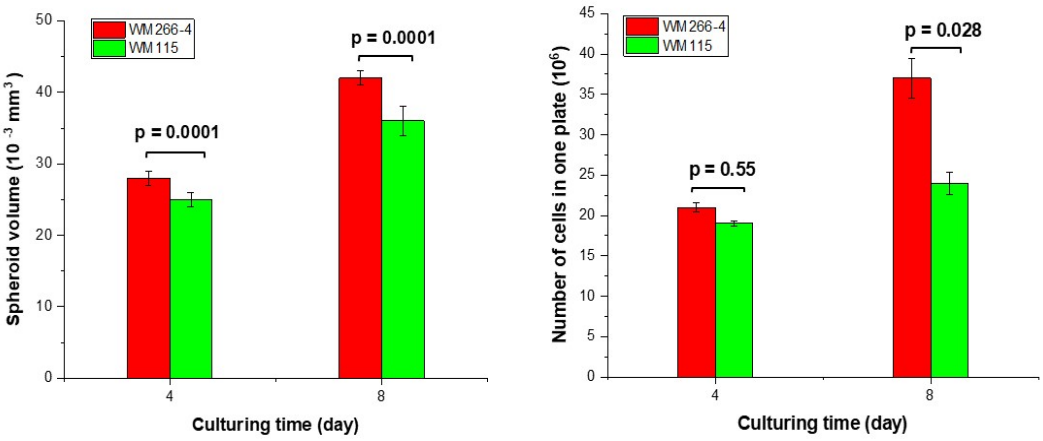

Figure 13.2: (left) The spheroids volume is increasing during the culturing time. WM266-4 spheroids have a faster proliferation than WM115 spheroids (p = 0.0001) due to their higher malignancy level. (right) The number of cells in a plate is increasing during the culturing time.

The viability tests have been evaluated before and after each PALS measurement. The test showed that spheroids viability has not changed significantly, 7.6% and 6.42% for WM266-4 and 2.37% and 4.03% for WM115 spheroids at day 4 and 8 days of culturing, respectively, Tab 13.1.

cell culture	day	viability(before)%	viability(after)%
WM266-4	4	88.6%(3.24)	81%(0.28)
	8	82.37% (2.61)	75.9%(1.34)
WM115	4	83.67%(1.62)	81.3 %(1.41)
	8	82.26%(1.53)	78.22%(3.05)

Table 13.1: Viability test has been checked before and after each PALS measurement to evaluate the effects of viability on o-Ps lifetime. The results show, viability of cells has not changed significantly during the measurement. Therefore it can no be considered as a parameter that can influence the o-Ps lifetime.

13.2 Spheroids' cells characterisation

WM266-4 spheroids with more metastasis characteristics had smaller cells in comparison to WM115 spheroids with less malignancy. The size of cells in 2D cell culture is also different than cells in 3D cell culture due to their different biological environment, Tab 13.2.

cell culture	day	WM266-4/cell size(μm)(SD)	WM115/cell size(μm)(SD)
3D	4	15.70(0.10)	16.66(0.20)
	8	15.92(0.08)	17.28(0.25)
2D		14.65(0.09)	16.27(0.1)

Table 13.2: The size of cells in WM266-4 and WM115 cell lines in the form of 3D and 2D cell culture.

The number of cells in both spheroids was growing during the time, Fig 13.2. The observed growth was faster for WM266-4 spheroids than for WM115 spheroids. The cells in WM115 spheroids had longer doubling time than cells in WM266-4 spheroids, around 7.5 and 6 days, respectively, which means WM115 cells spend longer time in their cell cycle with respect to cells from WM266-4 spheroids, Tab 13.3.

The population of cells in 2D cell culture can be estimated using Eq. 13.1, 13.2:

$$GR = \frac{ln\frac{(N_t)}{N_0}}{t} \tag{13.1}$$

$$DT = \frac{ln2}{GR}, \tag{13.2}$$

where the N_t is the number of cells at time t, N_0 is the number of cells at time 0 and GR is rate of growth [112].

cell culture	WM266-4/DT(day)	WM115/DT(day)
3D	6	7.5
2D	1.3	2.5

Table 13.3: Doubling time of WM266-4 and WM115 cell lines in the form of 3D and 2D cell culture.

13.3 The lifetime of o-Ps

The mean lifetime of o-Ps atoms in the spheroids was established for two different cell lines characterized with different degrees of malignancy. The obtained results given in Tab. 13.4 show that WM266-4 spheroids with higher proliferation rate, and concentration of cells have a shorter o-Ps mean lifetime than WM115 spheroids; therefore, the smaller free inter-molecular voids, than WM115 cells from the primary tumor with less division rate and lower concentration of cells over time. Although both cell lines show a decrease in the lifetime of o-Ps during the time of culturing, o-Ps show a longer lifetime in WM115 than in WM266-4 spheroids. The intensity of o-Ps in WM266-4 spheroids remained almost constant, while WM115 spheroids present a decrease in the o-Ps intensity, which can be considered as changes at the molecular level in WM115 spheroids cells. Figure 13.3 shows the exemplary experimental lifetime spectrum, WM266-4 and WM115 3D spheroids.

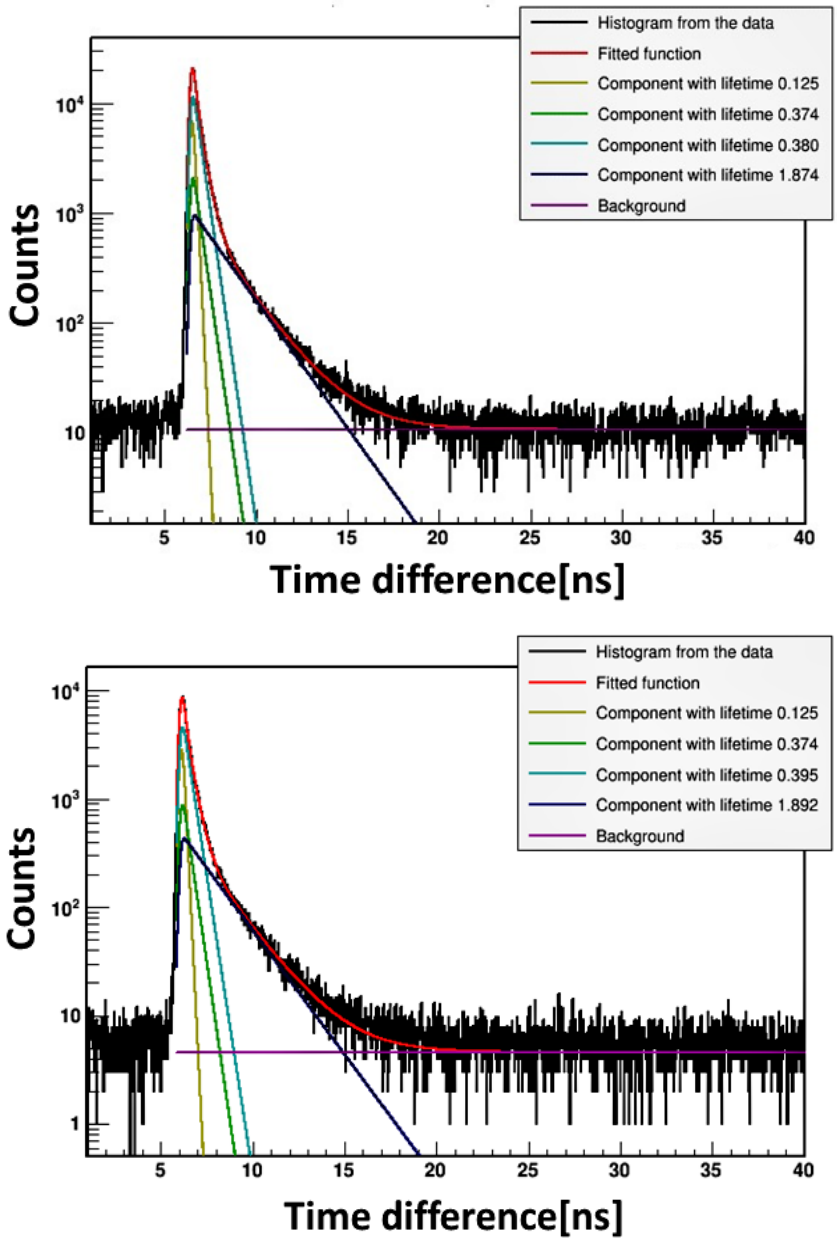

Figure 13.3: Exemplary experimental lifetime spectra for WM266-4 (upper) and WM115 (lower) spheroids. Black histogram indicates data and superimposed curves result from the fit of the sum of the exponential function convoluted with the detector resolution, performed by means of the PALS Avalanche program [96,99]. First component (yellow line) shows the lifetime of p-Ps, second component (green line) indicates the lifetime in source (Kapton foil), third component (light blue) shows free annihilation lifetime and forth component (dark blue) illustrates the lifetime of o-Ps. A sum of all contribution resulting from the fit is shown as a red curve.

The results for all components with the mean values have been calculated for WM266-4 and WM115 spheroids and are presented in Tab 13.4. The measurement uncertainty has been calculated as standard deviation. Figure 13.4 demonstrates the results of mean o-Ps lifetime and distribution in 3D melanoma spheroids with different malignancy levels at two different culturing times. It is interesting to note that the obtained o-Ps lifetimes are significantly larger than o-Ps lifetime in water at 37 °C which is equal to 1.78 ns [88].

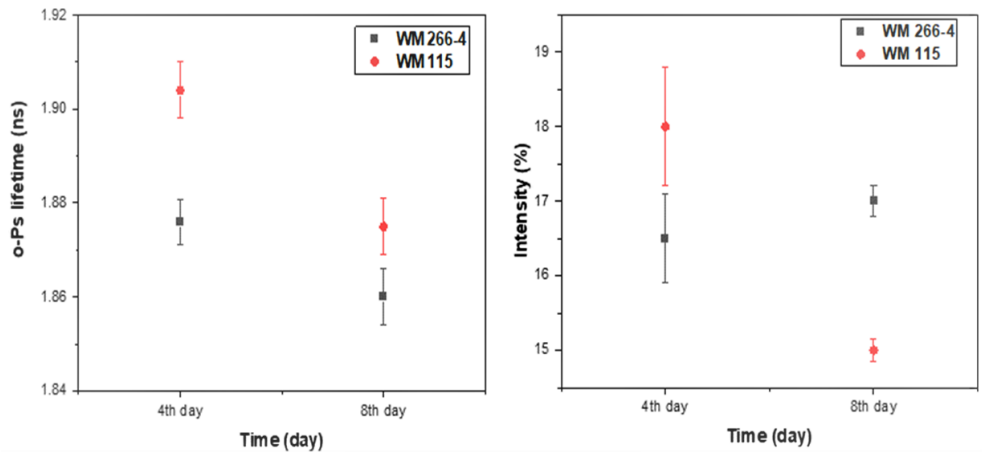

Figure 13.4: The lifetime and Intensity of o-Ps in WM266-4 and WM115 spheroids.

	$4^{th} day$	$8^{th} day$
	τ_{o-Ps}(ns), I(%)	τ_{o-Ps}(ns), I(%)
WM266	1.876(0.005), 16.5% (0.6)	1.861(0.006), 17.0% (0.2)
WM115	1.909(0.006), 18.0% (0.8)	1.875(0.006), 15.0% (0.2)

Table 13.4: Mean lifetime of o-Ps (τ_{o-Ps}) and o-Ps Intensity (I) in 3D melanoma spheroids without medium and chemical compounds.

Part IV

Discussion

Chapter 14

Discussion

14.1 Spheroid characteristics

Over the past decade, many efforts have been made to improve drug tests and therapeutic methods. One of the new approaches in the field of tumor and chemotherapy research is the use of 3D spheroids, which can potentially be a good replacement for using animal models and patient tissues because of their 3D architecture and establishment of cell-cell contacts [113]. An important aspect of medical and pharmacology studies is the need to comply with ethical guidelines and regulations. However, working with 3D spheroids established from cell lines can eliminate these and other limitations.
In normal cells, there is a phenomenon called contact inhibition which controls proliferation rate and cell growth. It is an anticancer mechanism that helps cells to transmit the signal to neighbors and avoid more collisions. In 3D cancer spheroids and real tumors, contact inhibition is lost and cells are under uncontrolled proliferation; cells do not notice the signals; therefore, they can grow on top of each other, unlike the normal cells and 2D cell cultures [114].

As mentioned before, cells in 2D cell culture have sufficient accessibility to nutrients and oxygen, whereas in 3D cell culture with a multi-layer structure, cells accessibility to necessary nutrients for survival depends on their distance from the surface. Due to enough accessibility to essential nutrients and basic needs, the doubling time in 2D cell cultures with homogeneous condition is faster than in 3D cell cultures with homogeneous condition. The malignancy degree can also affect cell cycle regulation. Cancer cells have different cell cycle regulation than normal cells affecting their division behavior [2].

The cell size and cell cycle time in 2D and 3D cell culture is different because cells in monolayer cell culture surrounded by homogeneous biological condition

and have sufficient accessibility to nutrients and oxygen while in 3D cell culture with a multilayer structure, cells are in different biological condition, and access to necessary nutrients for survival depends on their distance from the surface, Tab 13.3. 3D spheroids are spherical cellular aggregates in which the cells are in close contact with each other, mimicking *in vivo* conditions. Because of this similarity, spheroids can be used reliably to determine gene expression and cell biological characteristics [113, 115]. Since tumors start as a low density of cells, which then grow and proliferate, studies investigating the behavior of low cell densities in response to chemical and pharmaceutical stimulation can use spheroids as a convenient model to find more precise and reliable diagnostic and therapeutic approaches.

In this thesis, spheroids were cultured at different cell densities and their rate of growth and size were assessed throughout the culture. Utilizing 3D cell culture helps to control the size and volume of spheroids as a tumor model, as well as evaluate cancer cell behavior at different stages and under different conditions, which reflects their behavior of the real tumor.

The results of this thesis show that WM266-4 spheroids as a malignant cell line have a bigger diameter, more circularity and smaller cell size than WM115 spheroids with non-malignancy characteristics. The shape and size of spheroids depend on the rate of growth, spheroid generation method and the time of culturing. The spheroids become more concentrated and rounded during the culturing time.
The necrotic area increased in the center of a spheroid during the time of culturing. That necrosis was more significant in bigger spheroids than smaller spheroids due to higher numbers of cells and more competition between cells to use nutrients. My results continued to evaluate the spheroids characteristics using fluorescence imaging techniques. Melanoma cells contain a black pigment (melanin) or a red pigment (eumelanin); therefore it should be taken into account which stains are appropriate for melanoma spheroids. Calcein and FDA are water soluble dyes and their diffusion is limited to solvent penetration. Moreover, fluorescein emission signal is quenched by conjugation to biopolymers(melanin) and it is sensitive to pH changes: the strongest signal is observed at base pH (9.0) and the lowest at acidic conditions (5.0), which is expected in the inner compartments [116]. The results in this thesis showed, choosing suitable staining technique can help to visualize the proliferation rim and necrotic region in spheroids.
Usually, common fluorescent microscopy techniques are sufficient for most experiments using spheroids as a model, especially those from a single cell line.

Currently, different methods are applied to bring more insight concerning multicellular spheroid structure, e.g. optical coherence tomography (OCT), as refractive index (RI) has the potential to be used as a marker for the spheroid growth phase [117].
Micro-CT has already been successfully used for imaging animal tissues and biological samples but, in this thesis, it is shown that micro-CT can also be used to visualize and analyze spheroids in 3D. In contrast to microscopy methods, micro-CT allows for the reconstruction of the shape, surface, and internal structure of the spheroids in 3D. Similarly to OCT, micro-CT can become a complementary method for spheroid imaging. Spheroids are very sensitive to fixative and staining solutions and the best results were obtained after staining for 90 min with Lugol solution without fixation. In this study, comparisons between confocal and micro-CT models were not fully displayed, especially in terms of necrotic zone determination. For the more adequate necrotic core visualization, the more adequate contrasting agent should be used.
Presently, there is no such agent for necrotic cell visualization and there is a need for developing such a lipid-specific contrasting agent. Spheroids mimic major features of *in vivo* tumors, especially cell-to-cell interactions, and can model tumor environments [118]. Tissue differentiation and angiogenesis, for example in cardiac [119] or cancer spheroids [120] can be visualized by means of micro-CT technique, and this approach would be helpful to observe vessel formation and structure. Moreover, multiple object analysis is possible and very convenient. It speeds up the workflow.
The rate of glucose and oxygen uptake in spheroids with different malignancy levels is different. Malignant cell lines uptake more glucose due to higher growth rate and division; therefore the concentration and following consumption of glucose is higher. Owing to spheroid growth, cell number increases, and competition for essential nutrients arises between cells. For detection of hypoxia region in spheroids and tumors, different approaches have been applied such as fluorescence probes in bioluminescence imaging or radiolabled tracers in Single Photon Emission Computed Tomography (SPECT) or Positron Emission Tomography (PET) [81, 121]. The results show that the hypoxia region and necrotic core appear in the inner part of a spheroid. Hypoxia is a hallmark of malignancy and affects the cell survival. From the malignancy point of view, hypoxia can induce gene modification and enable cancer cells to grow, overcome and tolerate nutrient starvation. There is a direct relationship between malignancy and hypoxia. As results show, WM266-4 melanoma spheroids with higher malignancy levels exhibit a wider hypoxic area than WM115 spheroids,

Fig 12.6. My results confirmed the previous findings that hypoxia is an important physiological characteristic of a malignant tumor which induces tumor survival in deprivation condition and promotes tumor invasion as a responsive mechanism [122].

14.2 Positronium lifetime

The main aim of this study was to introduce the positronium for assessing the cancer properties. Since cancer begins from a small number of cells and grows gradually, small-sized 3D spheroids were considered to evaluate the o-Ps lifetime in melanoma cancer cell lines. The rate of growth and size of spheroids depend on the size and type of cavities in a plate that have been seeded. The bigger micro cavities, the bigger spheroids will be formed. Although the size of spheroids can be controlled by initial culture seeding, the scales of micro wells can also affect the spheroid diameter [123].
For the measurement of positronium lifetime in spheroids, two different types of melanoma spheroid, malignant (WM266-4) and primary tumor (WM115) in two different culturing times were selected. The rate of viability has been evaluated before and after each measurement. In my study, spheroids were dissociated to single-cell suspension using the Trypsinization procedure and this dissociation were done gently to not destroy the cells and achieve a precise viability rate. After 20 minutes in the incubator, the cells were checked to be sure there are no aggregates. After the viability test utilizing the cell counter, the cell cluster map has been evaluated to see the percentage of clusters. The only samples were chosen with a high percentage of dissociation, above 90%, according to the cluster map.

The o-Ps lifetime has become a common application to evaluate the free intra-molecular spaces. Free volumes play an important role in the dynamic process of the mobility of small molecules or ions across the membranes [89]. Many kinds of research have been done on cancer diagnosis utilizing positronium annihilation lifetime. The prior research on the positronium lifetime has been mostly done on the different types of cancer tissue such as skin, cardiac myxoma and colorectal cancer cells and 2D cell cultures [18, 69, 90, 124–128].
In this novel research, the lifetime of o-Ps has been evaluated in 3D spheroids rather than in 2D cell culture or in tissues. Although lots of research has been performed on PALS measurement in materials and biological samples, the research on PALS using 3D spheroids is limited to only one research work which determined the lifetime of o-Ps in 3D colorectal cancer cell aggregates with a

mixture of cells and collagen in comparison to the effect of a drug on the same cell line with the same condition [92].

My study has been conducted to evaluate the lifetime and distribution of o-Ps in WM266-4 and WM115 spheroids with different malignancy degrees in two different culturing times. During the time period, both spheroid cell lines showed a reduction in o-Ps lifetime which backs to the gradual cell proliferation rate in spheroids. This decrease in o-Ps lifetime indicates a reduction in molecular mobility due to the high concentration of cells in spheroids and some modifications in cell-cell interactions, cell surface, and signals between cells.

WM266-4 spheroids show less o-Ps lifetime in comparison to WM115 spheroids due to higher proliferation rate and malignancy level. Different factors can influence the spheroid's properties, such as the concentration of oxygen, uptake rate of glucose, etc. in different layers of a spheroid. Each parameter can have its effect on spheroid proliferation, division, migration, cell size, and free volumes between molecules and following that lifetime and distribution of o-Ps.

In my thesis, the size of cells in 3D cell culture was larger than in 2D cell culture before seeding the cell on a plate. This can happen because cells are passages when the cells get high confluency, and most cells are in the log phase. In this phase, cells are in a period after cell doubling, between M and G_1, therefore the size of cells is the smallest one. Since spheroids have a heterogeneous structure, depends on the region where cells are located, cells have different cell cycles. For instance, cells that are on the surface of spheroids are mostly in S, G_2, and M phase while cells in the quiescent layer are in the G_1 phase. The size of cells during the S, G_2, and M phases is bigger than cells in G_1 phase therefore, spheroids have bigger cells in the proliferation rim than central zones [129, 130].

In this thesis, since the presence of a large necrotic zone in bigger spheroids was undesirable, small spheroids were created to have a bigger proliferation zone. The ratio of surface to volume is bigger in smaller cells than larger cells. When the surface to volume ratio in cells is higher it means these cells have more surface to diffuse nutrients and oxygen and they can grow faster than bigger cells. Cells in WM266-4 spheroids are smaller but have more growth rate than WM115 cells, therefore the number of cells in one single WM266-4 spheroid is higher than in a WM115 spheroid. This high density of cells keeps the cells close together which causes a decrease in free spaces between cells.

My results can also explain different stages of cancer for example primary and malignant tumors. The lifetimes of o-Ps in the cell can be different from

the lifetime measured in the case when the cell is in the medium containing water, collagen, or other chemical compounds because the cell surface, cell growth, and the shape of cells can be changed. Therefore, in this research, only spheroids without medium, water, and any chemicals have been evaluated. As these results present, malignancy can affect the o-Ps lifetime. WM266-4 spheroids with a higher degree of malignancy show larger positronium decay rate than WM115 spheroids, therefore positronium has a shorter mean lifetime in WM266-4 spheroids than in WM115 spheroids, Fig. 13.4.
As long as spheroids grow, the number of cells and the diameter of spheroids increase gradually. The cancer cells in 3D cell culture have tissue-like morphology. When the normal cell structures such as cell-cell interaction, cell signaling, adhesion, and organelles alter to cancer cells, these modifications affect the molecular composition of cell, the size of free space between molecules; therefore positronium trapping probability can be influenced by these modifications. The lifetimes of o-Ps in the cellular environment can be changed due to the presence of water, collagen, or other chemical compounds. These substances can modify the cell surface, cell growth, and also the shape of cells. Therefore, in this research, only spheroids without medium, water, or any chemicals have been evaluated.

However, the mean lifetime of o-Ps can be considered as the size of pores in different materials, intensity is considered as the concentration of free volume. In this thesis, the Intensity of o-Ps in WM266-4 spheroids remained almost constant. It can be considered that the cell structure has not changed during the time of experiment while WM115 spheroids present a decrease in the intensity which can be considered as some modification in WM115 spheroids cells however it is difficult to evaluate the properties of cells by intensity changes because intensity can be easily influenced by many reactions in organic and inorganic materials such as some chemical compounds, ions or reactive groups [131].

In summary, the results show that the lifetime and intensity of o-Ps are useful parameters to differentiate between the cancer cell lines malignancy level and time of growth. The shorter the o-Ps lifetime is, the more malignancy and proliferation rate the cancer cells have. WM266-4 spheroids with higher malignancy level have the shorter o-Ps lifetime than WM115 with non-malignancy properties. Therefore o-Ps show high potential for differentiate between the malignant and non-malignant cancer cell lines.

Chapter 15

Conclusion

In conclusion, results show that the lifetime of o-Ps is a useful parameter to evaluate the properties of cancer cells, and micro-CT can be a complementary approach for a common optical technique to visualize spheroid morphology for determination of the 3D cancer spheroids characteristics. Utilizing 3D spheroids enables *in vitro* studies of cell aggregates with properties similar as *in vivo* tumors, with an anatomical and physiological structure allowing cancer biological studies in a cost-effective and fast method. According to the motivations and aims of this Ph.D. thesis explained in chapter 6, several outcomes can be considered:

1. Micro-CT imaging is approved, being a complementary approach to visualize the different types of 3D cancer spheroids with different cancer cell line characteristics. Owing to this thesis results, micro-CT can be considered as an appropriate imaging tool for 3D spheroid structure; however, the staining protocol needs some improvements to visualize the necrotic core.

2. The multilayered structure of real tumors in *in-vitro* 3D spheroids with different uptake of glucose and oxygen can be observed by microscopic images.

3. The main research hypotesis was confirmed. The thesis shows that positronium lifetime can be introduced as an appropriate parameter for the diagnosis of 3D melanoma spheroids in the malignant and benign stages. The o-Ps lifetime shows changes in two different 3D melanoma spheroids with different malignancy degrees during the culturing time. Although positronium application can be considered as a promising biomarker for cancer diagnosis, further investigation is needed for other probable parameters' effect on

positronium lifetime.

Bibliography

[1] Ewa Stępień, Hanieh Karimi, Bartosz Leszczyński, and Monika Szczepanek. Melanoma spheroids as a model for cancer imaging study. *Acta Phys. Pol. B*, 51(1):159–164, 2020.

[2] Marta Kapałczyńska, Tomasz Kolenda, Weronika Przybyła, Zajączkowska Maria, et al. 2D and 3D cell cultures–a comparison of different types of cancer cell cultures. *Arch Med Sci*, 14(4):910–919, 2018.

[3] Franziska Hirschhaeuser, Heike Menne, Claudia Dittfeld, Jonathan West, et al. Multicellular tumor spheroids: an underestimated tool is catching up again. *J. Biotechnol.*, 148(1):3–15, 2010.

[4] Elisabete C. Costa, André F. Moreira, Duarte de Melo-Diogo, Vítor M. Gaspar, et al. 3D tumor spheroids: an overview on the tools and techniques used for their analysis. *Biotechnol. Adv.*, 34(8):1427–1441, 2016.

[5] Leoni A. Kunz-Schughart, Marina Kreutz, and Ruth Knuechel. Multicellular spheroids: a three-dimensional in vitro culture system to study tumour biology. *Int. J. Exp. Pathol.*, 79(1):1–23, 1998.

[6] Hanna Vörsmann, Florian Groeber, Heike Walles, Silke Busch, et al. Development of a human three-dimensional organotypic skin-melanoma spheroid model for in vitro drug testing. *Cell Death Discov.*, 4(7):e719, 2013.

[7] Sonia Wróbel, Małgorzata Przybyło, and Ewa Stępień. The clinical trial landscape for melanoma therapies. *J. Clin. Med.*, 8(3):368, 2019.

[8] Chante Karimkhani, Adèle C. Green, Tamar Nijsten, Martin A. Weinstock, et al. The global burden of melanoma: results from the global burden of disease study 2015. *Br. J. Dermatol.*, 177(1):134–140, 2017.

[9] Conor Steward. Number of new melanoma of the skin cases per 100,000 population in europe in 2018, by country, https://www.statista.com/statistics/1225588/skin-cancer-cases-in-europe/, 2021.

[10] Ecis - european cancer information system, https://ecis.jrc.ec.europa.eu.

[11] Sung-Jan Lin, Shiou-Hwa Jee, Wen-Chu Hsaio, Shu-Jen Lee, and Tai-Horng Young. Formation of melanocyte spheroids on the chitosan-coated surface. *Biomaterials*, 26(12):1413–1422, 2005.

[12] Sylwia Orzechowska. *Fizykochemiczna charakterystyka mineralizacji struktur kolagenowych.* PhD thesis, Jagiellonian University, 2018.

[13] Iwona M. Tomaszewska, Bartosz Leszczyński, Andrzej Wróbel, Tomasz Gładysz, and Hal F Duncan. A micro-computed tomographic (micro-ct) analysis of the root canal morphology of maxillary third molar teeth. *Ann. Anat.*, 215:83–92, 2018.

[14] Bartosz Leszczyński. *Optymalizacja procedur badawczych w biomedycznych zastosowaniach mikrotomografii komputerowej.* PhD thesis, Jagiellonian University, 2016.

[15] Brian D. Metscher. MicroCT for comparative morphology: simple staining methods allow high-contrast 3D imaging of diverse non-mineralized animal tissues. *BMC Physiol.*, 9(1):1–14, 2009.

[16] Bartosz Leszczyński, Paulina Sojka-Leszczyńska, Dorota Wojtysiak, Andrzej Wróbel, and Roman Pędrys. Visualization of porcine eye anatomy by x-ray microtomography. *Exp. Eye Res.*, 167:51–55, 2018.

[17] Paweł Moskal, Bożena Jasińska, Ewa Ł. Stępień, and Steven D. Bass. Positronium in medicine and biology. *Nat. Rev*, 1(9):527–529, 2019.

[18] Paweł Moskal, Kamil Dulski, Neha Chug, Catalina Curceanu, et al. Positronium imaging with the novel multiphoton pet scanner. *Sci. Adv.*, 7(42):1–9, 2021.

[19] Paweł Moskal, Daria Kisielewska, Roman Shopa, Zuzanna Bura, et al. Performance assessment of the 2 γpositronium imaging with the total-body pet scanners. *EJNMMI Phys.*, 7(1):1–16, 2020.

[20] Celesta Fong, Aurelia W. Dong, Anita J. Hill, Ben J. Boyd, and Calum J. Drummond. Positron annihilation lifetime spectroscopy (PALS): a probe for molecular organisation in self-assembled biomimetic systems. *PCCP*, 17(27):17527–17540, 2015.

[21] Maria V. Liberti and Jason W. Locasale. The warburg effect: how does it benefit cancer cells? *Trends Biochem. Sci.*, 41(3):211–218, 2016.

[22] Veronique Del Marmol and Kyleigh Lipira. 2020 melanoma skin cancer report. https://www.melanomauk.org.uk/2020-melanoma-skin-cancer-report. 2020.

[23] Deevya L. Narayanan, Rao N. Saladi, and Joshua L. Fox. Ultraviolet radiation and skin cancer. *Int. J. Dermatol.*, 49(9):978–986, 2010.

[24] Marco Rastrelli, Saveria Tropea, Carlo Riccardo Rossi, and Mauro Alaibac. Melanoma: epidemiology, risk factors, pathogenesis, diagnosis and classification. *In vivo*, 28(6):1005–1011, 2014.

[25] Francesco Pampaloni, Nariman Ansari, and Ernst HK. Stelzer. High-resolution deep imaging of live cellular spheroids with light-sheet-based fluorescence microscopy. *Cell Tissue Res.*, 352(1):161–177, 2013.

[26] Shreya Raghavan, Maria R. Ward, Katelyn R. Rowley, Rachel M. Wold, et al. Formation of stable small cell number three-dimensional ovarian cancer spheroids using hanging drop arrays for preclinical drug sensitivity assays. *Gynecol. Oncol.*, 138(1):181–189, 2015.

[27] Wentao Shi, Jean Kwon, Yongyang Huang, Jifu Tan, et al. Facile tumor spheroids formation in large quantity with controllable size and high uniformity. *Sci. Rep.*, 8(1):1–9, 2018.

[28] Ines Müller and Dagmar Kulms. A 3D organotypic melanoma spheroid skin model. *J. Vis. Exp. JOVE-J VIS EXP*, (135):e57500, 2018.

[29] Edoardo Milotti, Vladislav Vyshemirsky, Michela Sega, and Roberto Chignola. Interplay between distribution of live cells and growth dynamics of solid tumours. *Sci. Rep.*, 2(1):1–10, 2012.

[30] https://app.biorender.com/biorender-templates, 2021.

[31] Ewa Stepień, Jadwiga Stanisz, and Włodzimierz Korohoda. Contact guidance of chick embryo neurons on single scratches in glass and on

underlying aligned human skin fibroblasts. *Cell Biol. Int.*, 23(2):105–116, 1999.

[32] Rose G. Harrison, Milton J. Greenman, Franklin P. Mall, and Criag M. Jackson. Observations of the living developing nerve fiber. *Anat*, 1(5):116–128, 1907.

[33] Ewa Stepien. *Factors influencing neurit outgrowth in vitro*. PhD thesis, Jagiellonian University, 1999.

[34] Francesco Pampaloni, Emmanuel G. Reynaud, and Ernst Stelzer. The third dimension bridges the gap between cell culture and live tissue. *Nat. Rev*, 8(10):839–845, 2007.

[35] Brendon M. Baker and Christopher S. Chen. Deconstructing the third dimension–how 3D culture microenvironments alter cellular cues. *J. Cell Sci.*, 125(13):3015–3024, 2012.

[36] Mina J. Bissell, Aylin Rizki, and Saira Mian. Tissue architecture: the ultimate regulator of breast epithelial function. *Curr. Opin*, 15(6):753–762, 2003.

[37] Anna Birgersdotter, Rickard Sandberg, and Ingemar Ernberg. Gene expression perturbation in vitro—a growing case for three-dimensional (3D) culture systems. *Sem Cancer Biol*, 15(5):405–412, 2005.

[38] Sourabh Ghosh, Giulio C. Spagnoli, Ivan Martin, Sabine Ploegert, et al. Three-dimensional culture of melanoma cells profoundly affects gene expression profile: A high density oligonucleotide array study. *J. Cell. Physiol.*, 204(2):522–531, 2005.

[39] Stefan Walenta, Joerg Doetsch, Wolfgang Mueller-Klieser, and Leoni A. Kunz-Schughart. Metabolic imaging in multicellular spheroids of oncogene-transfected fibroblasts. *J. Histochem. Cytochem.*, 48(4):509–522, 2000.

[40] Albert H. Owens, Donald S. Coffey, and Stephen B. Baylin. *Tumor cell heterogeneity: origins and implications*. Academic Press, 1982.

[41] James P. Freyer and Robert M. Sutherland. Proliferative and clonogenic heterogeneity of cells from EMT6/Ro multicellular spheroids induced by the glucose and oxygen supply. *Cancer Res.*, 46(7):3513–3520, 1986.

[42] John W. Sheridan and Jacinta Simmons. Studies on a human melanoma cell line: effect of cell crowding and nutrient depletion on the biophysical and kinetic characteristics of the cells. *J. Cell. Physiol.*, 107(1):85–100, 1981.

[43] Koki Ono, Shota Takigawa, and Katsuya Yamada. L-glucose: Another path to cancer cells. *Cancers*, 12(4):850–877, 2020.

[44] Harry Rudney. The utilization of l-glucose by mammalian tissues and bacteria. *Science*, 92(2379):112–113, 1940.

[45] Katsuya Yamada. Aberrant uptake of a fluorescent L-Glucose analogue (fLG) into tumor cells expressing malignant phenotypes. *Biol. Pharm. Bull*, 41(10):1508–1516, 2018.

[46] María M. Adeva-Andany, Noemi Pérez-Felpete, Carlos Fernández-Fernández, Cristóbal Donapetry-García, and Cristina Pazos-García. Liver glucose metabolism in humans. *Biosci. Rep.*, 36(6):e00416, 2016.

[47] Maria L. Macheda, Suzanne Rogers, and James D. Best. Molecular and cellular regulation of glucose transporter (GLUT) proteins in cancer. *J. Cell. Physiol.*, 202(3):654–662, 2005.

[48] Elena S. Reckzeh and Herbert Waldmann. Development of glucose transporter (GLUT) inhibitors. *Eur. J. Org. Chem.*, 2020(16):2321–2329, 2020.

[49] Jessica Sadler, Nia J. Bryant, Gwyn W. Gould, and Cassie R. Welburn. Posttranslational modifications of GLUT4 affect its subcellular localization and translocation. *Int. J. Mol. Sci.*, 14(5):9963–9978, 2013.

[50] Hyoung Sook Park, Ji Hye Kim, Bo Kyung Sun, Sun U. Song, et al. Hypoxia induces glucose uptake and metabolism of adipose-derived stem cells. *Mol. Med. Rep.*, 14(5):4706–4714, 2016.

[51] Archana M Navale and Archana N Paranjape. Glucose transporters: physiological and pathological roles. *Biophys. Rev.*, 8(1):5–9, 2016.

[52] Louise Chang, Shian-Huey Chiang, and Alan R Saltiel. Insulin signaling and the regulation of glucose transport. *Mol. Med.*, 10(7):65–71, 2004.

[53] Sébastien Bonnet, Stephen L. Archer, Joan Allalunis-Turner, Haromy, et al. A mitochondria K channel axis is suppressed in cancer and its

normalization promotes apoptosis and inhibits cancer growth. *Cancer cell*, 11(1):37–51, 2007.

[54] Kristian Thorsen, Tormod Drengstig, and Peter Ruoff. Transepithelial glucose transport and na+/k+ homeostasis in enterocytes: an integrative model. *Am. J. Physiol. Cell Physiol.*, 307(4):C320–C337, 2014.

[55] Christiane Brahimi-Horn, Johanna Chiche, and Jacques Pouysségur. Hypoxia and cancer. *J. Mol. Med.*, 85(12):1301–1307, 2007.

[56] Jiangping Xu, Guillermo Vilanova, and Hector Gomez. A mathematical model coupling tumor growth and angiogenesis. *Plos one*, 11(2):e0149422, 2016.

[57] Adrian L. Harris. Hypoxia—a key regulatory factor in tumour growth. *Nat. Rev*, 2(1):38–47, 2002.

[58] Peter Vaupel, Oliver Thews, and Michael Hoeckel. Treatment resistance of solid tumors. *Med. Oncol.*, 18(4):243–259, 2001.

[59] Rosa A. Cardone, Valeria Casavola, and Stephan J. Reshkin. The role of disturbed pH dynamics and the Na+/H+ exchanger in metastasis. *Nat. Rev*, 5(10):786–795, 2005.

[60] Stefan Walenta and Wolfgang F. Mueller-Klieser. Lactate: mirror and motor of tumor malignancy. *Semin Radiat Oncol*, 14(3):267–274, 2004.

[61] Richard Sullivan and Charles H. Graham. Hypoxia-driven selection of the metastatic phenotype. *Cancer Metastasis Rev.*, 26(2):319–331, 2007.

[62] SalcedaSand CaroJ. Hypoxia-inducible factor1α (hif-1α protein is rapidly degraded by the ubiquitin-proteasome system under normoxic conditions. its stabilization by hypoxia depends on redox-inducud changes. *J Biol Chem*, 272:22642–22647, 1997.

[63] Stuart R. Stock. *Microcomputed tomography: methodology and applications*. CRC press, 2019.

[64] Anton Du Plessis, Chris Broeckhoven, Anina Guelpa, and Stephan Gerhard Le Roux. Laboratory x-ray micro-computed tomography: a user guideline for biological samples. *Gigascience*, 6(6):gix027, 2017.

[65] Birger Tielemans, Kaat Dekoster, Stijn E. Verleden, Stefan Sawall, et al. From mouse to man and back: closing the correlation gap between imaging and histopathology for lung diseases. *Diagnostics*, 10(9):636, 2020.

[66] Bartosz Leszczyński, Martyna Śniegocka, Andrzej Wróbel, Roman Pędrys, et al. Visualization and quantitative 3d analysis of intraocular melanoma and its vascularization in a hamster eye. *Int. J. Mol. Sci.*, 19(2):332, 2018.

[67] Paul M. Gignac, Nathan J. Kley, Julia A. Clarke, Matthew W. Colbert, et al. Diffusible iodine-based contrast-enhanced computed tomography (diceCT): an emerging tool for rapid, high-resolution, 3D imaging of metazoan soft tissues. *J. Anat.*, 228(6):889–909, 2016.

[68] Pawel Moskal. Positronium imaging. In *2019 IEEE Nuclear Science Symposium and Medical Imaging Conference (NSS/MIC)*, pages 1–3. IEEE, 2019.

[69] Hong Min Chen, David Van Horn, and Yan Ching Jean. Applications of positron annihilation spectroscopy to life science. *DDF*, 331:275–293, 2012.

[70] Bożena Jasińska and Paweł Moskal. A new pet diagnostic indicator based on the ratio of 3γ and 2γ positron annihilation. *Acta Phys. Pol. B*, 48(10):1577–1583, 2017.

[71] Ming Fang, Nathan Bartholomew, and Angela Di Fulvio. Positron annihilation lifetime spectroscopy using fast scintillators and digital electronics. *Nucl. Instrum*, 943:162507, 2019.

[72] Paweł Moskal, Dominika Alfs, Tomasz Bednarski, Piotr Białas, et al. Potential of the j-pet detector for studies of discrete symmetries in decays of positronium atom-a purely leptonic system. *Acta Phys. Pol. B*, 509(47):509–536, 2016.

[73] Caroll Quarles, Vincent Jobando, and Paul Arpin. Positron annihilation lifetime and doppler broadening correlations for a variety of polymers, cross linked rubbers and organic liquids. *Nucl. Instrum B.*, 261(1-2):875–878, 2007.

[74] Ryan W. Siegel. Positron annihilation spectroscopy. *Annu. Rev. Mater. Sci.*, 10(1):393–425, 1980.

[75] Bożena Zgardzińska. Can tao-eldrup model be used at short o-ps lifetime? *Acta Phys. Pol. A*, 125(3):700–701, 2014.

[76] Sun J. Tao. Positronium annihilation in molecular substances. *J. Chem. Phys.*, 56(11):5499–5510, 1972.

[77] Morten Eldrup, David Lightbody, and John Neil Sherwood. The temperature dependence of positron lifetimes in solid pivalic acid. *Chem. Phys.*, 63(1-2):51–58, 1981.

[78] Meenhard Herlyn, Gloria Balaban, Jeannette Bennicelli, DuPont Guerry, et al. Primary melanoma cells of the vertical growth phase: similarities to metastatic cells. *JJNCI*, 74(2):283–289, 1985.

[79] Hanieh Karimi, Bartosz Leszczyński, Tomasz Kołodziej, Ewelina Kubicz, et al. X-ray microtomography as a new approach for imaging and analysis of tumor spheroids. *Micron*, 137(10):102917, 2020.

[80] Katsuya Yamada, Masanori Nakata, Naoki Horimoto, Mikako Saito, et al. Measurement of glucose uptake and intracellular calcium concentration in single, living pancreatic β-cells. *J. Biol. Chem.*, 275(29):22278–22283, 2000.

[81] Rashmi Kumari, Dhanya Sunil, Raghumani S. Ningthoujam, and Anil Kumar. Azodyes as markers for tumor hypoxia imaging and therapy: an up-to-date review. *Chem. Biol. Interact*, 307:91–104, 2019.

[82] Wen Piao, Satoru Tsuda, Yuji Tanaka, Satoshi Maeda, et al. Development of azo-based fluorescent probes to detect different levels of hypoxia. *Angew. Chem.*, 125(49):13266–13270, 2013.

[83] Yue Gao, Mingguang Li, Bin Chen, Zancong Shen, et al. Predictive models of diffusive nanoparticle transport in 3-dimensional tumor cell spheroids. *AAPS J.*, 15(3):816–831, 2013.

[84] Kostas Kostarelos, Dimitris Emfietzoglou, Alexandros Papakostas, Wei-Hong Yang, et al. Binding and interstitial penetration of liposomes within avascular tumor spheroids. *Int. J. Cancer*, 112(4):713–721, 2004.

[85] Petr Stepanov, Farida Selim, Serge Stepanov, Alexander Bokov, et al. Interaction of positronium with dissolved oxygen in liquids. *Phys. Chem. Chem. Phys.*, 22(9):5123–5131, 2020.

[86] Pawel Moskal, Daria Kisielewska, Catalina Curceanu, Eryk Czerwiński, et al. Feasibility study of the positronium imaging with the j-pet tomograph. *Phys. Med. Biol.*, 64(5):055017, 2019.

[87] Bożena Jasińska, Marek Gorgol, Marek Wiertel, Radoslaw Zaleski, et al. Determination of the 3\gamma fraction from positron annihilation in mesoporous materials for symmetry violation experiment with j-pet scanner. *arXiv preprint:1602.05376*, 2016.

[88] Katsushige Kotera, Tadashi Saito, and Taku Yamanaka. Measurement of positron lifetime to probe the mixed molecular states of liquid water. *Phys. Lett. A*, 345(1-3):184–190, 2005.

[89] Yan-Ching Jean and Hans J. Ache. Positronium reactions in micellar systems. *J. Am. Chem. Soc.*, 99(23):7504–7509, 1977.

[90] Guang Liu, Hongmin Chen, Lakshmi Chakka, Joseph E. Gadzia, and Yan C. Jean. Applications of positron annihilation to dermatology and skin cancer. *pss(c)*, 4(10):3912–3915, 2007.

[91] Yan C. Jean, Ying Li, Gaung Liu, Hongmin Chen, et al. Applications of slow positrons to cancer research: Search for selectivity of positron annihilation to skin cancer. *Appl. Surf. Sci.*, 252(9):3166–3171, 2006.

[92] Eneko Axpe, Tamara Lopez-Euba, Ainara Castellanos-Rubio, David Merida, et al. Detection of atomic scale changes in the free volume void size of three-dimensional colorectal cancer cell culture using positron annihilation lifetime spectroscopy. *PLoS One*, 9(1):e83838, 2014.

[93] Wenjin Chen, Chung Wong, Evan Vosburgh, Arnold J. Levine, et al. High-throughput image analysis of tumor spheroids: a user-friendly software application to measure the size of spheroids automatically and accurately. *J. Vis. Exp. JOVE-J VIS EXP*, (89):e51639, 2014.

[94] Tor Hildebrand and Peter Rüegsegger. A new method for the model-independent assessment of thickness in three-dimensional images. *J. Microsc.*, 185(1):67–75, 1997.

[95] Szymon Witold Niedzwiecki. *Double-strip prototype of polymer time-of-flight positron emission tomograph based on multi-level analog electronics*. PhD thesis, Jagiellonian University, 2019.

[96] Kamil Dulski. Pals avalanche: a new pal spectra analysis software. *Acta Phys. Pol. A*, 137(2), 2020.

[97] Kamil Dulski, Bozena Zgardzinska, Piotr Bialas, Czerwinski, et al. Analysis procedure of the positronium lifetime spectra for the j-pet detector. *Acta Phys. Pol. A*, 132(5):1637–1640, 2017.

[98] Kamil Dulski. Assembly and calibration of apparatus for positron annihilation lifetime spectroscopy. master thesis. 2016.

[99] Kamil Dulski, Steven Bass, Juti Chhokar, Neha Chug, et al. The j-pet detector—a tool for precision studies of ortho-positronium decays. *Nucl. Instrum. Methods Phys. Res. A*, 1008:165452, 2021.

[100] John R. Quinn. Development of a pattern recognition approach for analyzing flow cytometric data. 2006.

[101] Tomasz Bednarski, Eryk Czerwiński, Paweł Moskal, Piotr Białas, et al. Calibration of photomultipliers gain used in the j-pet detector. *Bio-Algorithms and Med-Systems*, 10(1):13–17, 2014.

[102] Harold F. Blum. Estimation of growth rates of tumors. *J. Natl. Cancer Inst*, 4:21–24, 1943.

[103] Anne Talkington and Rick Durrett. Estimating tumor growth rates in vivo. *Bull. Math. Biol.*, 77(10):1934–1954, 2015.

[104] Esmaeil Mehrara, Eva Forssell-Aronsson, Håkan Ahlman, and Peter Bernhardt. Specific growth rate versus doubling time for quantitative characterization of tumor growth rate. *Cancer Res.*, 67(8):3970–3975, 2007.

[105] Mordecai Schwartz. A biomathematical approach to clinical tumor growth. *Cancer*, 14(6):1272–1294, 1961.

[106] Joseph J Casciari, Stratis V Sotirchos, and Robert M Sutherland. Glucose diffusivity in multicellular tumor spheroids. *Cancer Res.*, 48(14):3905–3909, 1988.

[107] JJ Casciari, SV Sotirchos, and RM Sutherland. Mathematical modelling of microenvironment and growth in emt6/ro multicellular tumour spheroids. *Cell Prolif.*, 25(1):1–22, 1992.

[108] Xun Hu, Ming Chao, and Hao Wu. Central role of lactate and proton in cancer cell resistance to glucose deprivation and its clinical translation. *Signal Transduct. Target. Ther.*, 2(1):1–8, 2017.

[109] Jennifer Ferguson, Michael Smith, Isabel Zudaire, Claudia Wellbrock, and Imanol Arozarena. Glucose availability controls atf4-mediated mitf suppression to drive melanoma cell growth. *Oncotarget*, 8(20):32946, 2017.

[110] Kenneth Thomas. Angiogenesis. *Encyclopedia of Cell Biology*, 4:102–116, 2016.

[111] SR McKeown. Defining normoxia, physoxia and hypoxia in tumours—implications for treatment response. *Br. J. Radiol. Suppl.*, 87(1035):20130676, 2014.

[112] Anna Korzyńska and Marzena Zychowicz. A method of estimation of the cell doubling time on basis of the cell culture monitoring data. *Biocybern Biomed Eng.*, 28(4):75–82, 2008.

[113] Yu-suke Torisawa, Airi Takagi, Yuji Nashimoto, Tomoyuki Yasukawa, et al. A multicellular spheroid array to realize spheroid formation, culture, and viability assay on a chip. *Biomaterials*, 28(3):559–566, 2007.

[114] Alisha M. Mendonsa, Tae-Young Na, and Barry M. Gumbiner. E-cadherin in contact inhibition and cancer. *Oncogene*, 37(35):4769–4780, 2018.

[115] Norio Koide, Khosaku Sakaguchi, Yayoi Koide, Kenichiro Asano, et al. Formation of multicellular spheroids composed of adult rat hepatocytes in dishes with positively charged surfaces and under other nonadherent environments. *Exp. Cell Res.*, 186(2):227–235, 1990.

[116] Michael J. Doughty. ph dependent spectral properties of sodium fluorescein ophthalmic solutions revisited. *Ophthalmic Physiol Opt*, 30(2):167–174, 2010.

[117] Neelam Hari, Priyanka Patel, Jacqueline Ross, Kevin Hicks, and Frédérique Vanholsbeeck. Optical coherence tomography complements confocal microscopy for investigation of multicellular tumour spheroids. *Sci. Rep.*, 9(1):1–11, 2019.

[118] Iftikhar Ali Khawar, Jong Kook Park, Eun Sun Jung, Myung Ah Lee, et al. Three dimensional mixed-cell spheroids mimic stroma-mediated chemoresistance and invasive migration in hepatocellular carcinoma. *Neoplasia*, 20(8):800–812, 2018.

[119] Isaree Pitaktong, Cecillia Lui, Justin Lowenthal, Gunnar Mattson, et al. Early vascular cells improve microvascularization within 3d cardiac spheroids. *Tissue Eng. Part C Methods*, 26(2):80–90, 2020.

[120] Sajita Shah, Hyunsook Lee, Young Hwan Park, Eunkyeong Jeon, et al. Three-dimensional angiogenesis assay system using co-culture spheroids formed by endothelial colony forming cells and mesenchymal stem cells. *J. Vis. Exp. JOVE-J VIS EXP*, (151), 2019.

[121] Donald Chapman, Edward L. Engelhardt, Corinne C. Stobbe, Richard F. Schneider, and Gerald E. Hanks. Measuring hypoxia and predicting tumor radioresistance with nuclear medicine assays. *Radiother Oncol.*, 46(3):229–237, 1998.

[122] Sergej Osinsky, Michael Zavelevich, and Peter Vaupel. Tumor hypoxia and malignant progression. *Exp. Oncol.*, 31(2):80–86, 2009.

[123] Yusuke Sakai and Kohji Nakazawa. Technique for the control of spheroid diameter using microfabricated chips. *Acta Biomater.*, 3(6):1033–1040, 2007.

[124] Petri Sane, Filip Tuomisto, Susanne K. Wiedmer, Tuula Nyman, et al. Temperature-induced structural transition in-situ in porcine lens—changes observed in void size distribution. *Biochim Biophys Acta*, 1798(5):958–965, 2010.

[125] Yin Chuan-Yuan, Guo Dong-Lin, Xi Tao, Xu Xian-Xiu, and Gu Qing-Chao. Studies on structural features of human tumor necrosis factor. *Nucl sci tech*, 8(4):218–218, 1997.

[126] Bożena Jasińska, Bożena Zgardzińska, Gustaw Chołubek, Marek Gorgol, et al. Human tissue investigations using pals technique: free radicals influence. *Acta Phys. Pol. A*, 132(5), 2017.

[127] Bożena Jasińska, Bożena Zgardzińska, Gustaw Chołubek, Marek Pietrow, et al. Human tissue investigations using pals technique: free radicals influence. *Acta Phys. Pol. A*, 132(5):1556–1558, 2017.

[128] Pawel Moskal, Ewelina Kubicz, Grzegorz Grudzien, Eryk Czerwinski, et al. Developing a novel positronium biomarker for cardiac myxoma imaging. *bioRxiv*, 2021.

[129] Miriam B. Ginzberg, Ran Kafri, and Marc Kirschner. On being the right (cell) size. *Science*, 348(6236):771–882, 2015.

[130] Kimberley A. Beaumont, Andrea Anfosso, Farzana Ahmed, Wolfgang Weninger, and Nikolas K Haass. Imaging-and flow cytometry-based analysis of cell position and the cell cycle in 3d melanoma spheroids. *J. Vis. Exp. JOVE-J VIS EXP*, (106):53486, 2015.

[131] Bożena Jasińska and Bożena Zgardzińska. New porosimetric method based on the 3γ annihilation rate. applications to materials science and medical imaging. *Acta Phys. Pol. A*, 132(5):1616–1619, 2017.